

INTERDISCIPLINARY DOCTORAL SCHOOL

Faculty of Electrical Engineering and Computer Science

Kamal MARANDSKIY

Remote Sensing Data Analysis for Earth Observation Applications

SUMMARY

Scientific supervisors

Prof. Dr. Mihai IVANOVICI and Prof. Dr. Fabio DEL FRATE

BRAȘOV, 2025

Contents

1	Introduction	3
1.1	Remote Sensing	3
1.2	Precision Agriculture	4
1.3	Machine Learning	4
1.4	Soil Surface Roughness	4
1.5	Soil Moisture	5
1.6	Plant Schematics	5
1.7	Hyperspectral Image Visualization and Compression	6
1.8	Early Detection of Crop Fields	6
2	Soil Roughness	7
2.1	Chain Method	7
2.2	Pinboard Method	7
2.3	Preliminary Experiments	7
2.4	Digital Imaging of Laser-Projected Patterns for Soil Surface Roughness Estimation	8
2.4.1	Image Data Collection and Processing	9
2.4.2	Experimental Results	10
2.5	Estimating Soil Surface Roughness from Soil Digital Images Using Fractal Analysis	10
2.5.1	Image Acquisition and Preprocessing	10
2.5.2	Experimental Results	10
2.6	Fractal Analysis of Multispectral Soil Surface Images from Different Altitudes	11
2.6.1	Data Acquisition and Processing	12
2.6.2	Experimental Results	13
3	Soil Moisture	15
3.1	Methodology	15
3.1.1	Simplified IEM	15
3.1.2	Numerical Surface Generation	16
3.1.3	Moisture Content of the Soil	17
3.1.4	IEM Data and CNN	17
3.2	Results and Discussions	17
4	Plant Schematics	19
4.1	Methodology and Data	19
4.2	Results	21
5	Hyperspectral Imaging: Visualization, Classification and Compression	22
5.1	Hyperspectral Image Visualization	22
5.1.1	Experimental Results	22
5.2	Exponential Feature Extraction and Learning for Pixel-Wise Hyperspectral Image Compression	24
5.2.1	Experimental Results	25
6	Crop Type Identification	27
6.1	Early Identification of Potato Fields Using Data Fusion and ANN	27
6.1.1	Experimental Results	27
7	Conclusion	29

Acknowledgement

Firstly, I thank to my supervisor Prof. Mihai Ivanovici for his scientific contribution to my Ph.D. as well as his support for giving me opportunity to be part of AI4AGRI project. His continuous encouragement to attend workshops, summer schools, conferences, scientific mobilities and more, greatly improved my skills and widened my knowledge. He established the Romanian Excellence Center on AI for Agriculture and I became one of the first people who contributed to it. I thank to my co-supervisor Prof. Fabio Del Frate for his guidance and scientific advice. He invited me to join mobility programs at EO Lab in Tor Vergata University of Rome and helped me to advance in my studies. We hope our research will further improve this initiative and lay foundations for future researchers.

I thank to my advisory board members, Prof. Corneliu Florea, Conf. Angel Cataron, Conf. Radu-Mihai Coliban, and Dr. Serban Oprisescu for their intellectual contribution and guidance. I also thank to my colleague Dr. Stefan Popa for his help at various steps of the research mainly, at data collection, technical advice and practical knowledge for writing the thesis. I thank to Transilvania University of Brasov and its rector Prof. Ioan Vasile Abrudan for providing scholarship and creating opportunity for research and study during my Ph.D. program. I thank to all the Professors who taught me important subjects at the beginning of the program.

I thank to my parents and my family for their encouragement, endless support and understanding, even though I had been far away from them. I especially thank to my lovely partner Nemuutsetseg for being on my side all along, providing me with support and care.

This work is funded by the European Union. The AI4AGRI project entitled Romanian Excellence Center on Artificial Intelligence on Earth Observation Data for Agriculture received funding from the European Unions Horizon Europe research and innovation programme under grant agreement no. 101079136.



**Funded by
the European Union**

Chapter 1

Introduction

1.1 Remote Sensing

Remote Sensing (RS) is the process of acquiring information about an object or phenomenon without a physical contact typically by measuring its reflected and emitted radiation using specialized sensors on satellites or aircraft. RS is a set of tools and techniques that allow the analysis of physical characteristics of Earth or other planetary bodies. Tools that are used in RS can be divided into two categories: active and passive sensors. Active sensors relies on emitting electromagnetic signals and receiving the reflected portion from the objects. Based on the time that signal takes to travel and/or the characteristic of the returned signal, certain information about the object and the medium can be assessed. Common technology examples for this principle are microwave emitting radar (radio detection and ranging) instruments and infrared light emitting lidar (light detection and ranging). Main form of a radar system is Synthetic Aperture Radar (SAR) that uses motion of the attached platform to synthetically expand the aperture of the radar. SAR has unique capability which is penetrability that allows it to see 'through' clouds and capture images. Microwave portion of the electromagnetic spectrum is affected by the dielectric constant (which is correlated with the water content of plants and soil), surface roughness, the sensor's incidence angle, and physical structure of the objects. Copernicus is the Earth Observation (EO) component of the European Union's Space program and under it, Sentinel-1 mission is SAR equipped satellites providing global coverage of Earth and data is free to use.

Multispectral and hyperspectral imagers are the major examples of the passive optical instruments. Multispectral instruments capture <30 bands covering from visible to infrared part of the electromagnetic spectrum through optical filtering techniques. The optical assembly directs incoming light through dichroic mirrors or fixed bandpass filters, that separate the light into a limited number of spectral channels. The light is then detected by specialized sensor arrays, such as CCDs or CMOS detectors, which convert the optical signal into an electrical one with a high degree of radiometric accuracy. The processed data results in separate image layers for each spectral band. The Copernicus Sentinel-2 mission delivers high-resolution optical imagery for terrestrial monitoring. Multispectral instrumentation capturing data across 13 spectral bands from visible to short-wave infrared wavelengths. It is effective in analysis of vegetation, water bodies, soil characteristics, and land cover dynamics. Hyperspectral imaging starts with capturing light across a continuous range of wavelengths, the system uses optical dispersion elements, such as prisms or diffraction gratings, to separate the incoming light into its component wavelengths. The resulting spectral dispersion is recorded by high-density focal plane arrays, which commonly use pushbroom scanning techniques to capture one spatial line at a time along with the complete spectrum for each pixel. It allows for the creation of a three-dimensional data structure known as hypercube. Both multispectral and hyperspectral data plays an important role in the assessment of the vegetation layer in agricultural settings.

1.2 Precision Agriculture

Agriculture is the main source of food for the majority of the population, however, such demand creates stress on agricultural lands. It results in excessive usage of lands, thus, degradation in soil quality, weaker crops, poor yield production, etc. Besides human activity, climate also affects crop growth mainly drought, flood, cold snap, etc. Most negative influences on crops can be prevented or accounted for if detected in the early stages. Such prevention is possible if fields are monitored constantly. RS is a core technology in precision agriculture, SAR is actively used in soil moisture (SM) analysis, biomass estimation, yield prediction, etc. Another important pillar of modern agriculture is sustainability and efficiency. Water management is critical, as precision irrigation systems utilize spatial and temporal data to apply the right amount of water to different field zones based on SM conditions and crop requirements. This maximizes the efficient use of water and improves water scarcity in drier areas. Similarly, fertilizers and pesticides can be applied variably according to the specific needs of different field sections, reducing both costs and potential environmental harm. On the other hand, multispectral and hyperspectral data is used for crop health monitoring, disease detection, etc. The main example is a handcrafted feature called the Normalized Difference Vegetation Index (NDVI) that quantifies the greenness of the vegetation and it relies on near-infrared and red bands. In complex cases, satellite data is integrated with ground-based sensors and even with unmanned aerial vehicles (UAV) for decision-making. Beyond these, energy usage and labor can also be optimized with automated machinery and smart scheduling.

1.3 Machine Learning

A huge amount of data is generated daily by Sentinel missions satellites under the Copernicus program. Useful information can be extracted and used in various applications including agriculture. Machine learning (ML), specifically the sub-branch, deep learning (DL), has been an important research area in the last decade and can be applied to various industries. This became possible due to the improvements in parallel computing and more efficient and powerful hardware units. This review paper will focus on methods and techniques in ML to classify crop fields using RS data. Machine learning algorithms can be categorized into supervised learning, unsupervised learning, semi-supervised learning, and reinforcement learning. Our studies extensively utilize DL methods specifically, Convolutional Neural Networks (CNNs) and fully connected Artificial Neural Networks (ANNs) to extract meaningful patterns from the vast amounts of Sentinel data. These techniques are particularly adept at handling the high-dimensional and complex nature of earth observation imagery. A detailed review of ML algorithms and applications in agriculture is discussed in a dedicated chapter.

1.4 Soil Surface Roughness

Soil surface roughness (SSR) is a critical physical characteristic that describes the irregularities present on the soil surface. These irregularities result from inherent soil properties including texture, aggregate size, and the presence of rock fragments sand from anthropogenic activities such as tillage and other land management practices. Thus, soil roughness is shaped by both the natural microtopography of soil and the modifications imposed by agricultural or mechanical interventions[1]. In the literature, SSR is often quantified by statistical measures such as the standard deviation (SD) of surface heights over a defined area. Fundamentally, SSR is too small to be captured by topographic mapping or digital elevation models, which is why it is also known as soil micro-topography. SSR significantly affects SAR backscatter by modulating the scattering mechanisms. Rough surfaces generally increase backscatter, which can mask the dielectric effects of SM. Therefore, accurately quantifying surface roughness is essential to isolate and retrieve SM signals from SAR data in RS applications. Various indices have been developed to describe types of SSR that are formed by different natural phenomena or human activities: (1) Micro-relief variations or grain roughness, primarily influenced by the soil type; (2) Random roughness (RR), associated with soil aggregates; (3) Oriented roughness, representing systematic topographical variations

caused by factors such as tillage; and (4) Higher-order roughness, accounting for elevation changes within the field, and field borders. In our studies, we focused on the RR and we performed experiments around it. Two classical methods were used for SSR estimation, chain and pinboard methods. We tested their effectiveness in lab and in situ measurements. Images of the laser-projected surfaces taken with the Canon 5D Mark II from a distance. In order to estimate the SSR we used a type of ANN called CNN, ResNet-18 [2] to be specific. The advantage of this approach is its simplicity and low cost. Experiments were conducted with four different artificial surfaces and real soil in the lab and assessed the potential of the approach over classical methods.

We proposed the fractal analysis (FA) method to quantify the fractal dimension (FD) of the digital images of the soil surface. Classical methods are limited to the 1D measurements while fractal analysis gives complexity analysis in 2D dimensional space. We developed our own setup that blocks illumination and creates a controlled acquisition environment. Data was collected from bare soil of agricultural field in collaboration with the National Institute of Research and Development for Potato and Sugar Beet, Brasov, Romania (NIRDPSB). Beyond RR and small variations in the soil which is important for interpreting SAR backscattering, we also experimented with the drone images of the bare soil surfaces which were taken with a multispectral camera that has five bands. Experiments were conducted at 60m and 80m altitudes and we analyzed how complexity develops as we increase the number of bands and altitude. 'Bird-eye' view of the agricultural fields and FA of the multispectral images have the potential to quantify the global SSR.

1.5 Soil Moisture

SM is the water content of the soil. The spatial and temporal distribution of water stored on the land is a key parameter controlling various processes as well as affecting others in the climate system. SM and atmosphere interactions have significant impacts on the water and energy cycle, trace gases, including carbon dioxide, especially, considering vegetation layers [3], [4]. Water has natural circulation, it evaporates, changes from liquid to gas form, then eventually, recondenses as liquid. Water absorbed by plants during photosynthesis becomes part of carbohydrates in plants, which turns into water again via decomposition. The complex interaction of water and atmosphere coupling, accompanied by various vegetation and land compositions make SM a critical factor in understanding and modeling Earth's climate system, agricultural productivity, and ecosystem health. Its influence extends from local plant growth to global climate patterns. Predicting SM with RS technologies has been an active research area in the last few decades.

Electromagnetic models, particularly surface radar backscatter models, are designed to simulate interactions between the radar signal and target and, by inverting them, estimation of parameters like SM and SSR is possible. We used the Integral Equation Model (IEM) to generate a dataset along with simulated Gaussian-correlated surface profiles that include varying SSR and SM parameter values and encoded them into computer-generated color images which are the inputs for the CNN model. Backscattering estimations for vertical-vertical (VV, co-polarized) and vertical-horizontal (VH, cross-polarized) polarization channels from IEM simulation were used as target variables in the CNN model. Moreover, with the foundation of this research, we plan to integrate more complex scenes and eventually replace computer-generated, synthetic images with real ones.

1.6 Plant Schematics

In the context of SAR, ground, and plant interaction, we conducted multiple field campaigns and collected data on the physical features of the wheat crops such as dimensions of the leaves and height of the crops. Data was later used to create computer-generated drawings of the wheat and soil. We used the computer-generated schematics to classify the crop growth stages and associated SAR backscattering values.

1.7 Hyperspectral Image Visualization and Compression

One of the main challenges in hyperspectral images (HSI) is the visualization of HSI due to the fact that HSI contains from tens to hundreds of bands but the screens we are using display only three bands namely: red, green, and blue. There are various ways to visualize HSI and a significant amount of research has been done. Depending on the focus of the application, visualization methods can be chosen, while some methods focus on the most natural selection of red, green, and blue (RGB), others focus on highlighting the different materials in the scene. Furthermore, these methods can be categorized based on the general technique involved. The literature classified them into five categories namely: band selection-based, principal component analysis (PCA)-based, linear, based on digital image processing techniques, and machine/deep learning-based methods [5]. We propose a method to map the dominant wavelength (λ) from each pixel to RGB triplet and we utilize a lookup table of RGB values per wavelength between 380 : 781nm. Each surface such as water bodies, vegetation, and bare soil has a unique signature of the reflected light, thus, we make the assumption that certain bands in the reflected radiation have a dominant one that may reveal information about the scene when it is displayed. It is a pixel-wise approach and has the advantage of being simple by emphasizing the most reflective band while for the same reason, the disadvantage is that it utilizes only one band and discards the rest.

Detailed spectral information in HSIs makes them versatile and useful, however, it also results in large data sizes. One of the challenges in hyperspectral imaging is to efficiently transfer and store data while preserving spectral and spatial information. Various HSI compression methods have been proposed, we can categorize them into transform, prediction, learning, and vector quantization-based methods [6]. It is also common to divide them into two classes: lossless and lossy compression. We propose a lossy compression technique and it relies on two fundamental hypotheses: first, that negative exponential functions adequately approximate Fourier spectra of hyperspectral pixel reflectance profiles; second, that ANNs can effectively learn mappings between these negative exponential representations and actual spectral reflectance curves. This negative exponential formulation captures essential spectral characteristics while eliminating redundant information, resulting in substantial data volume reduction. Our second hypothesis leverages recent ML advancements demonstrating ANNs' capacity to recognize and model complex data relationships.

1.8 Early Detection of Crop Fields

Identification of the crop types in agricultural settings is an active research area and tackles challenges such as crop shortfalls, yield prediction, assessment, mitigation, and adaptation decisions [7]. Considering the data-heavy nature of satellite imagery, one of the effective ways to extract useful information is by using ML and particularly sub-branch, DL models. Such models, especially, complex ones (deeper neural networks) are capable of exploring and extracting useful information from multimodal data sources and making use of spatial, spectral, and temporal features along with being adaptable to the changes in the environment [8]. Ground ridging process on the potato fields in particular results in distinct patterns. Many studies focused on the identification of the fields during their growth season where crop features directly contribute to the NDVI that can be detected with multispectral camera [9]. However, only a few studies considered such ridging patterns to be useful. In one such study, UAV is deployed for data collection, and gray-level co-occurrence matrix was used as a texture feature which significantly improved the classification accuracy [10]. Some studies used the temporal aspect of crop rotation from five or more years and predicted the incoming year's crop map, which relies on the past rotation patterns rather than actual characteristics of the field [11]. We propose an approach based on the combined usage of multispectral and SAR data to identify the potato after ridging and before the crop growth.

Chapter 2

Soil Roughness

2.1 Chain Method

This method provides a 1D measurement of the soil profile and it is an inexpensive way of measuring the SSR. The chain roughness (Cr) is the ratio between the distance on the surface ($L_1 = 1m$) over the Euclidean distance (L_2) that is measured by the ruler. Cr is calculated as [12]: $Cr = \left(1 - \frac{L_2}{L_1}\right) \times 100$. Figure 2.1 a) shows the usage of a chain with a ruler in one of the field campaigns.

2.2 Pinboard Method

The pinboard method is commonly used for determining the RR index. In Allmarass (1966) [13] formulation, roughness is quantified as the natural logarithm of the SD calculated from multiple height measurements after removing biases such as slope, directional roughness, or the top and bottom 10% of the data. Later, Cremers et al. (1996) [14] suggested that correcting solely for slope effects suffices, a definition we have adopted here. Our constructed pinboard spans a 73cm wide frame and features 53 aluminum pins which are later replaced with black wooden ones, each 33 cm tall, spaced 10 mm apart, and 3 mm in diameter. Data was captured using a Canon 5D Mark II, as shown in Figure 2.1.

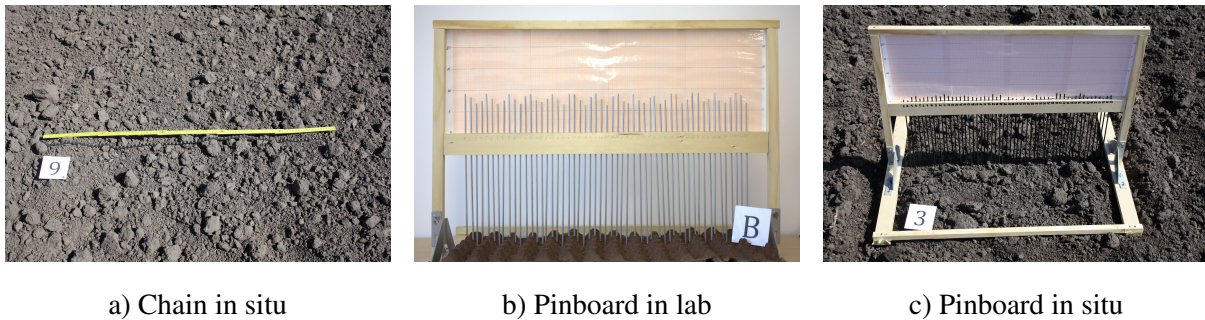


Figure 2.1: Application of chain and pinboard setups.

2.3 Preliminary Experiments

Preliminary experiments were conducted in the lab with the synthetic surfaces (a) flat, (b) regular, (c) quasi-regular, and (d) irregular (2.2). A flat surface was used to measure the error of pinboard setup which is a result of uneven pin heights and it is approximately 1mm for metal pins and less for wooden ones. This is due to the fact that metal pins were manually cut and the process introduced imperfections. We measured the surface roughness of the artificial surfaces using the pinboard and chain method. Table 2.1 shows the result where SD of pin heights in pinboard and Cr are directly a measure of SSR. * indicates

that measurements were performed exactly on the same line meaning pinboard pins were placed right on top of the chain. We also performed measurements without placing the pins on top of the chain, but simply using the same line on the surface and we obtained a correlation over 90%. In order to calculate the Pearson Correlation Coefficient (CC) we need to have multiple points of measurement for each method and they must be obtained from the same line over the surface. However, the real soil surface is less deterministic, especially, on a small scale where pins and chains contact. This is one of the main drawbacks of these methods, the other one is the fact that we only capture a single dimension (1D). Even though measurements were performed at multiple points on the given field, numbers can vary greatly, thus, we explored the potential of FA and FD as SSR.

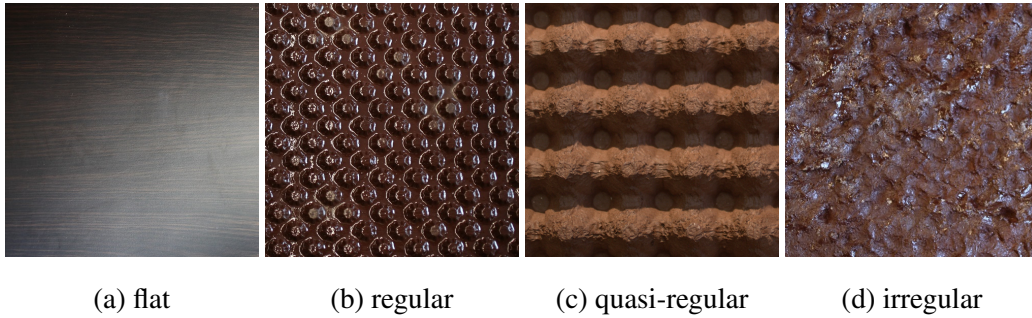


Figure 2.2: Artificial soil surfaces [15].

Table 2.1: SD and C_r of artificial soil surface samples [15].

Name	Sample A	Sample B	Sample C	Sample D
C_r	0	6.57	25.29 (16.52)	2.44
C_r^*	0	7.5	15.03 (13.91)	2.1
SD	0.094	0.27	1.01 (0.92)	0.35
SD*	0.094	0.31	0.52 (0.58)	0.29

2.4 Digital Imaging of Laser-Projected Patterns for Soil Surface Roughness Estimation

Similar to the working principles of SAR, Terrestrial Laser Scanning is an active sensor sending millions of light pulses instead of microwaves, then receiving the reflected discrete data points. By measuring the time-of-flight for each data point, it measures the X, Y, and Z coordinates of each. Another method that relies on light beams is laser profilometry which does not use time-of-flight instead uses camera and optical triangulation methods to extract a 3D profile of the surface. It has a high spatial resolution, analyzing surfaces in finer details, but is usually, limited to confined areas. Inspired by laser profilometry we propose an approach that uses a simple red light emitting laser horizontally over the sample surfaces and it allows to closely profile the surfaces. This approach is closer in principle to laser profilometry, however, it lacks spatial resolution and does not use any triangulation methods for a detailed 3D map of the surface. Additionally, images of the laser-projected surfaces are taken with the Canon 5D Mark II from a distance, but they can also be taken with any decently capable camera that clearly captures the laser pattern. In order to estimate the soil roughness we used a type of ANN called CNN, ResNet-18 [2] to be specific. The advantage of this approach is its simplicity and low cost.

2.4.1 Image Data Collection and Processing

We have projected laser over artificial surfaces (Figure 2.2) and a real soil surface inside the laboratory. Figure 2.3 shows the sample images, it is important to note that we captured multiple profiles of each surface except the flat one. Starting with the first row which is a cropped version of the actual scene since the camera pointed at 30° was capturing a wider area, the second row shows a grayscale version of the images while the third row shows a binarized form which isolates the laser pattern from the background. Table 2.2 shows the roughness of artificial surfaces and real soil. In total, we have five surfaces but six classes because in the case of the quasi-regular surface we obtained different SSR values when pins were placed on towers and cups of egg cartons, thus, the quasi-regular surface resulted in two classes. Even though other surfaces except the flat one were slid under the pinboard and laser line, we did not obtain a significant difference in SSR value.

Flat	Regular	Quasi-regular	Irregular	Real soil
0.094	0.271	1.011, 0.922	0.347	0.826

Table 2.2: SSR values of artificial and real soil, measured with pinboard.

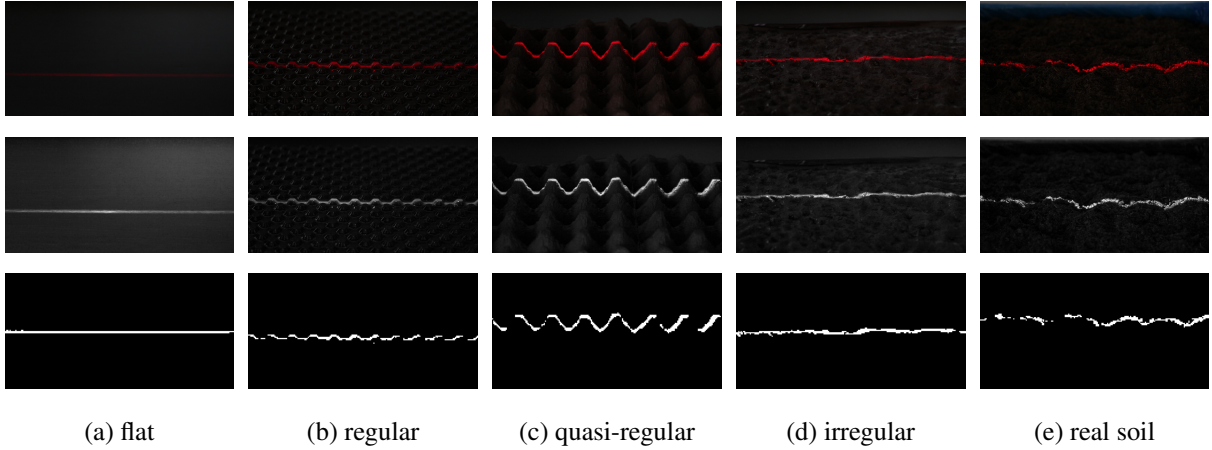


Figure 2.3: Samples cropped from RGB images of the projections of a red laser line over the surfaces (1st row), grayscale (2nd row), black and whitebinarized (3rd row) [16].

In order to increase the robustness of the ANN, we adopted multiple image augmentation techniques. Overall, they can be divided into two procedures: i) noise augmentation; ii) image transformation. Even though initial images were binary, in order to perform noise augmentation images must have continuous values. Image augmentation is also an effective approach to increase the number of samples, in our case, from 27 to 972.

ResNet-18 CNN

Resnet-18 CNN solves the vanishing gradient problem of deep neural networks by leveraging residual (skip) connections. Gradients computed during backpropagation can become very small ("vanish") as they move backward through each layer. As a result, weight updates in early layers become very minimal or even stalls. Residual blocks in ResNet create a shortcut, where instead of direct mapping of input x to output with the function $H(x)$, each block learns $F(x)$ residual function, thus, the final output becomes $H(x) = x + F(x)$. This process allows gradients to flow more easily towards the initial layers allowing the network to perform well even in deeper layers. We used the Pytorch library to utilize ResNet-18 which is 18 layers deep, pre-trained on the ImageNet dataset and we modified the final layer to classify the laser profile images into six classes. In our experiments, we trained the network using the Adam optimizer [17] and the cross-entropy loss function.

2.4.2 Experimental Results

Results of the training and validation indicate that the model can easily learn from laser patterns and map them to the SSR. Considering the limited amount of surface samples, we tackled the problem as a classification task, but in the case of data availability, the problem can be shaped as a regression, and expect the model to predict continuous output of SSR values. Two types of graphs were considered in interpreting the results, progress graphs and confusion matrices. Progress graphs show loss and accuracy against epochs both for training and validation, while confusion matrices show a number of correctly classified and misclassified samples which indicates how good the model is in terms of per class accuracy. Our dataset has a class imbalance but we did not explicitly use any loss function to counter it. Across the five folds, the model achieved a training accuracy as high as 99.74% (with a loss of 0.0160 in one instance) while consistently maintaining a perfect validation accuracy of 100% (with a validation loss as low as 0.0037).

2.5 Estimating Soil Surface Roughness from Soil Digital Images Using Fractal Analysis

In 1983, Mandelbrot introduced the concept of fractal geometry as a means to describe self-similar sets, now commonly known as fractals [18]. A central parameter in this framework is the FD, which quantifies the complexity and degree of space occupancy of these irregular structures. Although the Hausdorff fractal dimension provides a rigorous theoretical foundation for continuous objects, its practical application is limited by its abstract formulation.

The method described in [19] was used as a foundation and we adapted it to work with 2-dimensional gray-scale images and 1-dimensional signals. 2D images of the soil surface were cropped and resized from the much bigger image of real soil surface images from agricultural fields, down to 256×256 sized area of interest. We also extracted 1D lines with the size of 1×256 from the given image and averaged it and it is called the average profile (AP). Which can be formulated as follows: $AP = \frac{1}{N} \sum_{i=1}^N l_i$ where, l_i - is the i th line of each image. In experiments in [20], researchers used sliding pinboard and averaged the measurements to increase the precision of the 1D acquisition, thus, we took a similar approach in fractal analysis and estimated fractal dimension of 1D AP of digital soil surface images.

2.5.1 Image Acquisition and Preprocessing

Natural illumination has significant effects on in situ image acquisition, the sun's position during the day can cast shadows or brightness can change depending on the azimuth angle and clouds. It is important to maintain consistent illumination conditions for reliable measures. We developed a 'black box' setup as described in Figure 2.4 that isolates the RoI from outer light while providing artificial illumination from inside using controlled LED strips. The camera hole is designed to let the lens part enter completely while maintaining minimum intervention. We used the same Canon 5D Mark II digital camera for laser profile experiments which has 21 megapixels providing sufficient resolution. We acquired a total of 12 images at different locations inside a large agricultural field. Images need to be preprocessed before applying FA, and the steps are as follows: RGB images were converted to grayscale eliminating color information; each image was cropped 7 times in overlapping fashion to increase the number of samples for correlation analysis, and resized to 256×256 . Pixel brightness was also adjusted for every image ensuring even more consistency between images. We obtained a total of 84 images after preprocessing steps.

2.5.2 Experimental Results

A regression analysis was carried out in parallel with determining the Pearson CC for three distinct data sets: in situ measurements, reference methods (chain and pinboard), and the fractal analysis of image crops. Although laboratory results from the reference methods were highly correlated, practical application did not reveal a correlation between the chain and pinboard methods which is likely due to

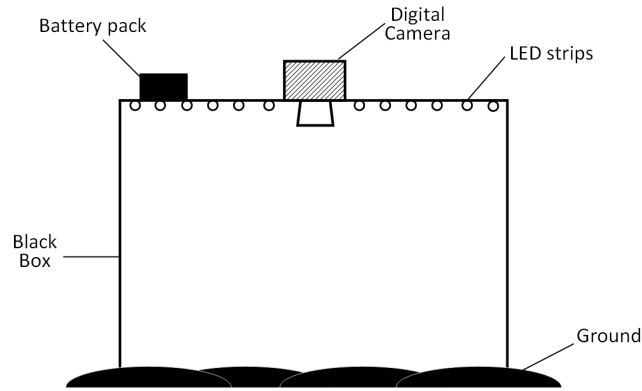


Figure 2.4: Block diagram describing box setup that is used for image acquisition [15].

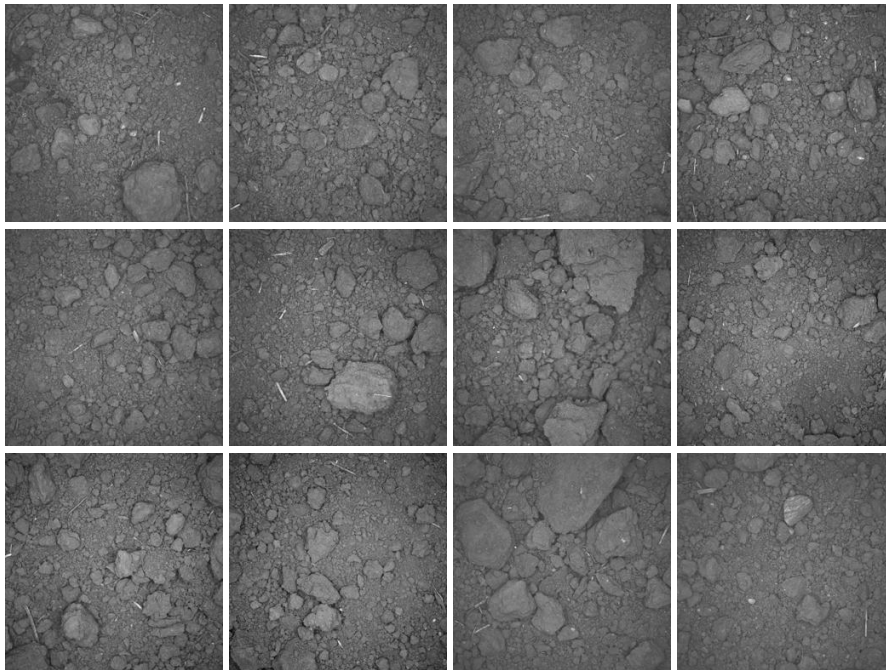


Figure 2.5: Soil surfaces preprocessed imagettes that were taken at 12 different locations and used for FA [15].

discrepancies in ground measurement lines. The maximum correlation between the reference methods and the fractal analysis was 0.34. In Figure 2.6 we show the data and the regression line for the pinboard measurements and the FD of the 84 imagettes representing soil surface digital images (left) and the chain measurements and the FD of the AP of the 12 images corresponding to the 12 measurement locations (right).

2.6 Fractal Analysis of Multispectral Soil Surface Images from Different Altitudes

We further explored FA of bare soil surfaces in order to quantify SSR. While in the previous section, we used an invasive method by placing a box over the soil surface, in this section we focus on a "bird-eye" view of the agricultural fields in the case of bare soil. SSR is a complex parameter and depending on the spatial resolution it can provide various insights. Depending on the application, resolution and the areal coverage may vary. The previous method was aimed towards RR and played an alternative approach to

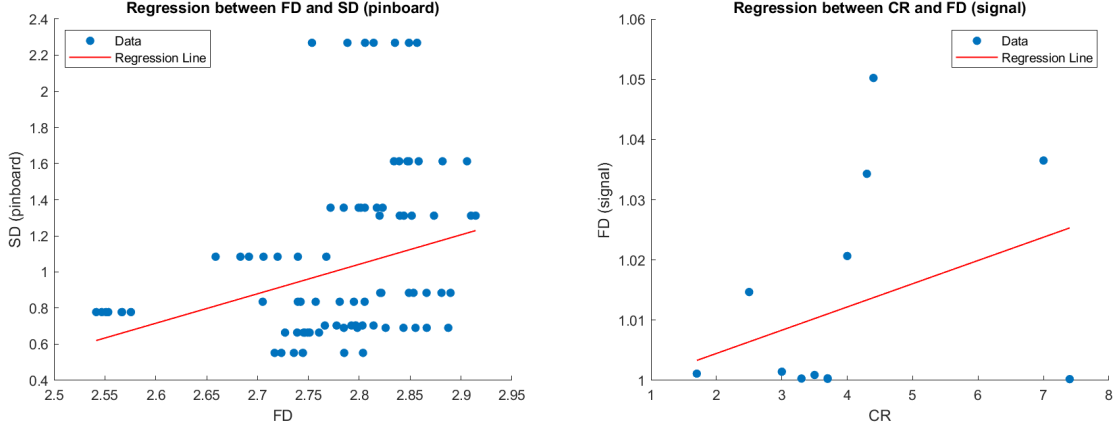


Figure 2.6: Correlation analysis for pinboard and FD of 84 image crops of soil surface digital images ($CC=0.34$) and chain and FD of 12 image APs ($CC=0.33$) [15].

traditional methods such as pinboard and chain, which captures smaller variations in the soil surface and helps to understand microwave (SAR acquisitions) interaction with the surface. On the other hand, it is also important to understand soil surface complexity from a much higher view, especially, for applications based on lower-resolution spaceborne SAR instruments. To tackle this aspect we used UAV attached multispectral camera that captures a total of five bands across visible and near-infrared spectrum. FA has a wide spectrum of applications such as signals, images, textures, structures, etc. [21]. In this section, the multispectral FD estimator method from [22] was adopted and adapted to five-band multispectral image analysis.

2.6.1 Data Acquisition and Processing

The Trinity F90+ UAV equipped with MicaSense RedEdge-MX multispectral camera was employed for data acquisition. This high-performance drone features carbon fiber construction with a great durability-to-weight ratio, integrating brushless propulsion systems alongside navigation components including GPS, gyroscopes, and accelerometers. It is autonomous and executes predetermined flight paths while maintaining precise altitude control and complex pattern completion with minimal human oversight due to its advanced navigation capabilities. The platform supports multiple communication protocols, allowing remote operation. Weather resistance and extended flight time make it suitable for agricultural sensing applications in variable field conditions. The integrated MicaSense RedEdge-MX represents advanced multispectral imaging technology specifically engineered for precision agricultural analysis and environmental assessment. The sensor delivers high-resolution spectral data critical for vegetation health monitoring, stress identification, and biomass evaluation across diverse ecosystems. Its optical system incorporates five precisely calibrated narrowband sensors capturing discrete wavelength ranges: blue, green, red, red-edge, and near-infrared spectral bands. Each band provides distinct and rich information regarding plant physiological status, with particular sensitivity to chlorophyll content, cellular structure, and water content variations across vegetation canopies. The system's radiometric calibration ensures consistent measurements across varying illumination conditions.

Before applying FA, images needed to be preprocessed starting with normalization of the pixel intensity values between 0 – 255, further, five spectral band images (grayscale) were aligned using SURF feature detection algorithm [23] where the red-edge image was used as a reference because its sensor is located in the center of the camera. Considering that FA algorithm works effectively with 256×256 sized images, we took a total of 12 non-overlapping crops from each image and Matlab was used to perform all the preprocessing steps. FA was applied on grayscale (individual bands), RGB images, grayscale images converted from RGB, and complete multispectral images with five bands.

2.6.2 Experimental Results

Smart Intuitive Drones SRL conducted the acquisition campaign over an agricultural field at Transilvania University of Brasov's R&D Institute (coordinates: 45.669340, 25.550753). The top row of Figure 2.7 shows three cropped RGB images that were acquired at 60m altitude while the bottom row presents RGB images that were acquired at 80m altitude. Figure 2.8 (a) shows the FD value distribution of grayscale images converted from RGB color images. One can notice that the FD distribution of grayscale images acquired from different altitudes shows a slight distinction while in RGB ones (Figure 2.8 (b)) the difference is more prominent since it was expected because RGB images have higher complexity in comparison to the grayscale ones. Figure 2.9 Finally in multispectral image FD distribution at 60m and 80m again shows higher complexity compared to the grayscale and RGB.

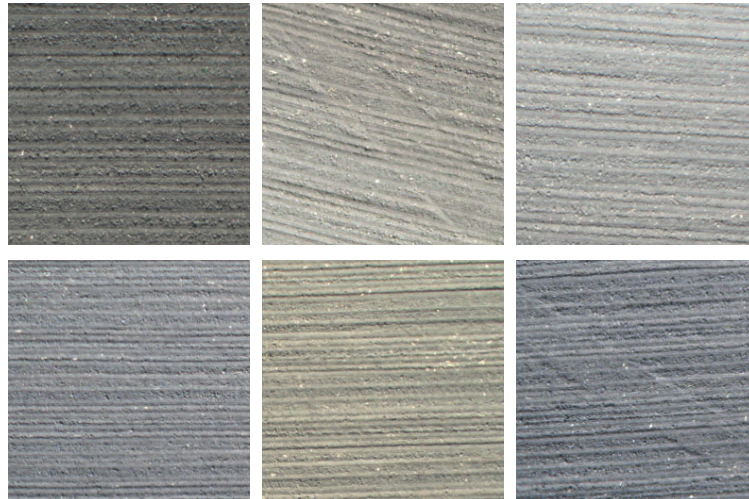
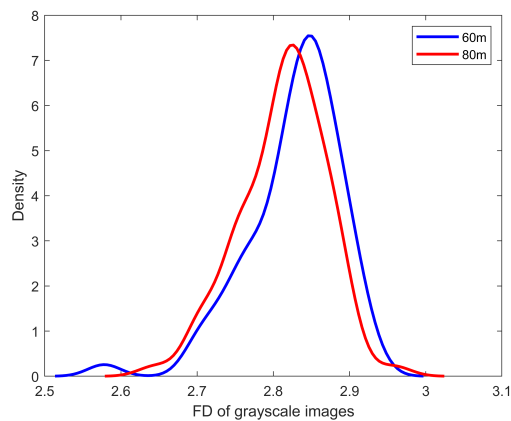
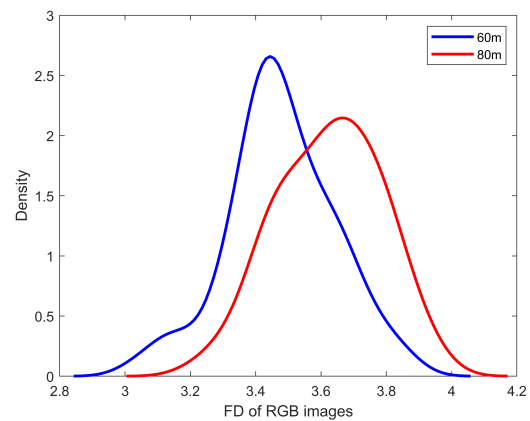


Figure 2.7: Cropped RGB images from 60m (top row) and 80m (bottom row) altitudes [24].



(a) Grayscale images (converted from RGB)



(b) RGB images

Figure 2.8: Distribution of FD values for images captured at 60m and 80m altitudes: (a) grayscale images (converted from RGB) and (b) RGB images [24].

Table 2.3 shows the average and spread of the FD values from the histograms in Figures 2.8 (a) and (b), and 2.9. FD tends to climb as the spectral resolution and altitude increase, and the mean (μ) provides a quick snapshot of these shifts. Notice that the mean for the grayscale images is nearly identical for 60m and 80m, hinting that single-band images might not capture all the nuances of the soil surface. Since these images were taken over a broad field in different spots, the FD mean can serve as a representative

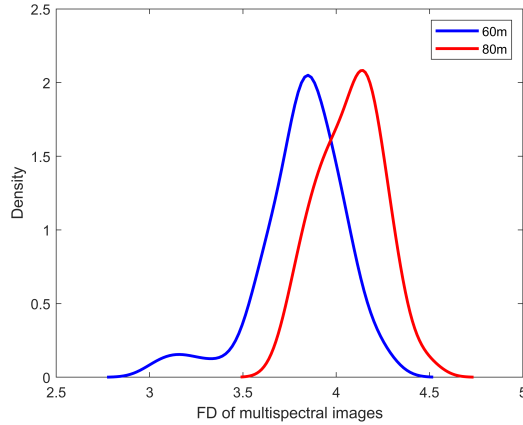


Figure 2.9: Distribution of FD values of multispectral images from 60m and 80m altitudes [24].

value for RR. Additionally, the consistently low SD (σ) across all settings suggests that the FD values are quite uniform.

	Grayscale		Color		Multispectral	
	μ	σ	μ	σ	μ	σ
60 m	2.83	0.06	3.48	0.16	3.82	0.23
80 m	2.81	0.056	3.62	0.16	4.07	0.17

Table 2.3: Mean (μ) and SD (σ) of FD values of grayscale, color, and multispectral images from 60m and 80m altitudes [24].

Two key insights emerged from our study. First, adding more spectral bands raises the estimated image complexity for a given ground scene. In fact, while grayscale (panchromatic) images failed to show any difference between 60m and 80m, both color and 5-band multispectral images did reveal such differences. Second, we found that soil complexity and by extension the SSR estimate is higher at 80m, even though we initially expected otherwise. This occurs because, at greater altitudes, ground details shrink, which increases the number of high-frequency elements in the Fourier spectrum and, in turn, increases complexity. For future studies, we plan to investigate a broader range of altitudes to better understand their impact on image complexity and SSR estimation, examine the effects of spectral mixing due to the sensors spatial integration, and assess the NIR bands role in SSR estimation.

Chapter 3

Soil Moisture

Two main parameters affect the reflected radar backscattering: i) the geometrical properties of the scene and ii) the dielectric constant. In SAR applications for bare soil, these properties can be described by SSR and SM parameters, since SSR is related to the variability of surface geometric features, and SM is strictly linked to the dielectric constant of the soil [25].

Electromagnetic models, particularly surface radar backscattering models, are designed to simulate interactions between the radar signal and target and, by inverting them, estimation of parameters like SM and SSR is possible. These models can be divided into three categories: empirical, semi-empirical, and physics-based [26]. Empirical approaches, like the one adopted in the Dubois model [27], and semi-empirical ones, such as the Oh models [28] rely on extensive ground-truth data for calibration. The physics-based models are IEM [29] and derived versions of it such as IEM_B by Baghdadi [30], and the Advanced Integral Equation Model [31].

In this study, we generated Gaussian-correlated surface profiles that include varying SSR and SM parameter values, and encoded them into computer-generated color images which are the inputs for the CNN model. Backscattering estimations for vertical-vertical (VV, co-polarized) and vertical-horizontal (VH, cross-polarized) polarization channels from IEM simulation were used as target variables in the CNN model. Moreover, with the foundation of this research we plan to integrate more complex scenes and eventually replace computer-generated, synthetic images with real ones.

3.1 Methodology

Research is formulated around two questions: 1) can we develop an efficient ML approach while achieving high accuracy to replace computationally intensive and complex IEM to predict SAR backscattering from bare soil surfaces?; 2) how does the representation of SSR and SM as image data, rather than scalar parameters, impact the ML model's ability to capture backscattering in different radar polarizations?

The scientific reasoning behind the methodology: i) while physics-based models like IEM, are accurate in many cases [32], they are complex to adjust and adapt to different scenarios; ii) representing SSR and SM as images allows CNNs capture their inherently spatial nature and complex patterns, preserving the spatial relationships; iii) image representations create a framework for future research to include vegetation layer and temporal changes while being intuitive and explainable. The methodology includes bare soil image schematics generation with varying SSR and SM values and predicting backscattering values with IEM simulation. Further, images are used as input to the CNN, and backscattering values from the IEM simulation are used as target values (see Figure 3.1).

3.1.1 Simplified IEM

IEM is based on Maxwell equations that considers boundary conditions between two media, in agricultural case it is often soil and vegetation layer. When SSR is relatively small compare to the wavelength then perturbation expansion is used where scattered field is expressed as a series. IEM is a physics-based

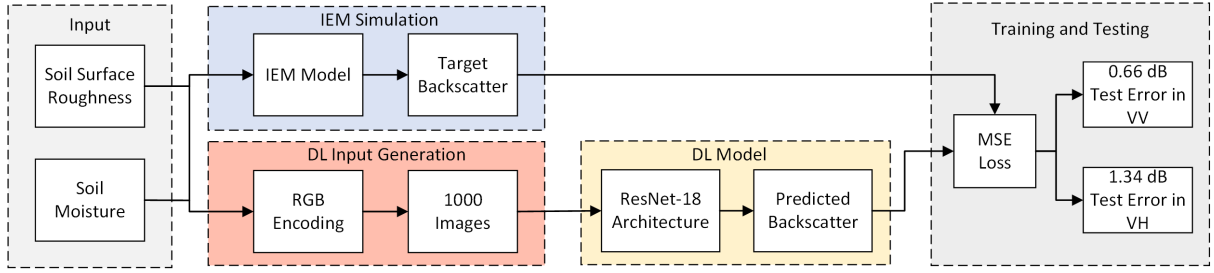


Figure 3.1: Block diagram of the proposed approach.

model and respects to fundamental principles such as energy conservation and reciprocity. Below is the simplified IEM for co-polarized case based on book chapter by A. K. Fung and K. S. Chen (2010) [32]. Other polarization cases and details for different scenarios can be found in the reference. The general forms of the backscattering coefficients for vertically, σ_{vv}^0 , horizontally, σ_{hh}^0 , and cross-polarized, σ_{vh}^0 , are given below.

$$\sigma_{pp}^0 = \frac{k^2}{4\pi} \exp[-2k^2\sigma^2 \cos^2 \theta] \sum_{n=1}^{\infty} |I_{pp}^n|^2 \frac{w^{(n)}(2k \sin \theta, 0)}{n!} \quad (3.1)$$

3.1.2 Numerical Surface Generation

IEM simulation expects statistically known surfaces such as Gaussian or Exponential surfaces and they usually closely resembles the natural surfaces. In this study we utilized Gaussian-correlated surface because its autocorrelation function (ACF) is correlated with the pinboard-measured soil surface profiles that we collected in previous field campaign with correlation of $R^2 = 0.88$. Two important parameters are used to describe SSR in case of surface simulations namely, root mean square of surface heights (σ) and correlation length (l) σ parameter describes the vertical surface height variations while l is to capture the horizontal profile of the surface. We closely followed the technique described in [33] to generate a Gaussian-like surface. l can be calculated where the autocorrelation function drops to $1/e$ (approximately 0.368) of its maximum value, a point where surface heights become decorrelated. The lag distance in spatial autocorrelation refers to the physical separation between pairs of observations in space. Figure 3.2. illustrates the two surface profiles over a distance ($L = 200$), where surface A represents a rougher surface ($\sigma = 2$) than surface B ($\sigma = 0.7$) and $l = 4$ in both cases. Toi parametrii suprafeei sunt în centimetri (cm).

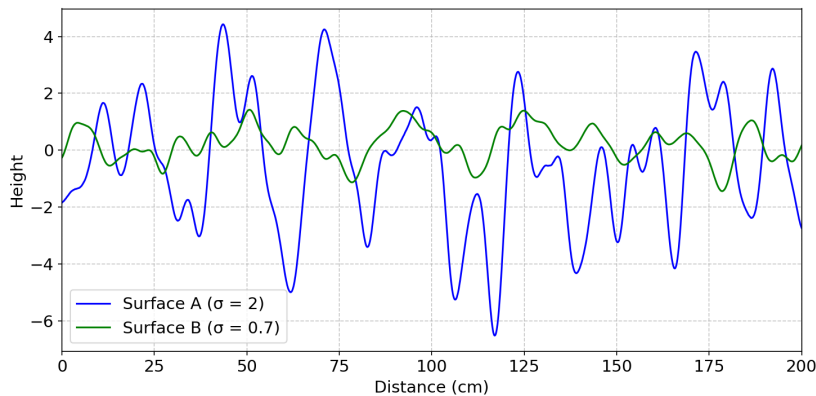


Figure 3.2: Two sample surface profiles with $\sigma = 2$ and $\sigma = 0.7$.

3.1.3 Moisture Content of the Soil

Soil dielectric permittivity is a key parameter in SAR simulation because it directly correlates with SM content [34], [35]. In our IEM simulation and as an input to the CNN model, we varied the SM from 1% to 50% in 1% increments. When representing bare soil data as images, the moisture content is encoded through color: light brown indicates dry soil, and dark brown indicates wet soil (see Figure 3.3).

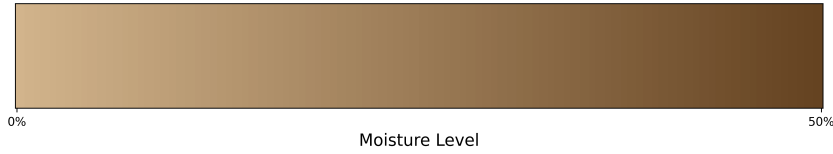


Figure 3.3: SM content is coded using a color gradient from light beige to deep brown, representing SM resolution from 0% to 50% saturation.

3.1.4 IEM Data and CNN

IEM data was generated using IEM simulation and it contains 50 moisture values from 1% to 50% for each SSR value from 0.1 to 2, totaling 1000 estimated VV and VH backscattering values each, further, these values were used as target variables in CNN. We used CNN, particularly, a deep residual learning with, ResNet-18 which overcomes the vanishing gradient problem and is mainly designed for image classification tasks [2]. However, by modifying the last layer it was adapted for the regression task. It is important to note that two independent ResNet-18 models were used to predicting one specific output (VV and VH) because single model performed less accurate when predicting two outputs. Moreover, after encoding the SSR and SM values into the images, they were resized to $224 \times 224 \times 3$ and split into training and testing with 80% and 20% respectively. The model uses the mean squared error (MSE) loss function, Adam optimizer with a learning rate of 0.001, and the model is trained over 50 epochs.

3.2 Results and Discussions

Figure 3.4 shows the generated bare soil synthetic images with various SSR and SM. Figure 3.5 shows how the training and test loss progress over 50 epochs. The MSE loss drops sharply during the early epochs, and the close proximity between training and test losses suggests that the model converges well without overfitting. Table 3.1 shows the composite score value at the best model, along with the training and test losses.

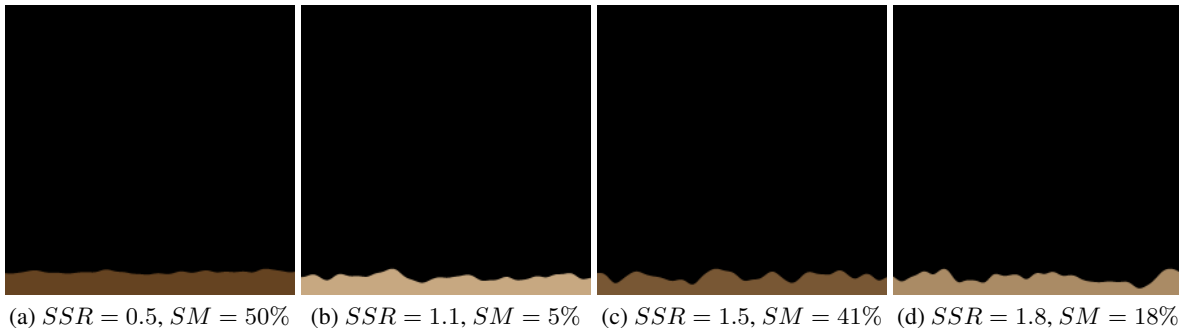


Figure 3.4: Generated bare soil synthetic images with various SSR and SM levels.

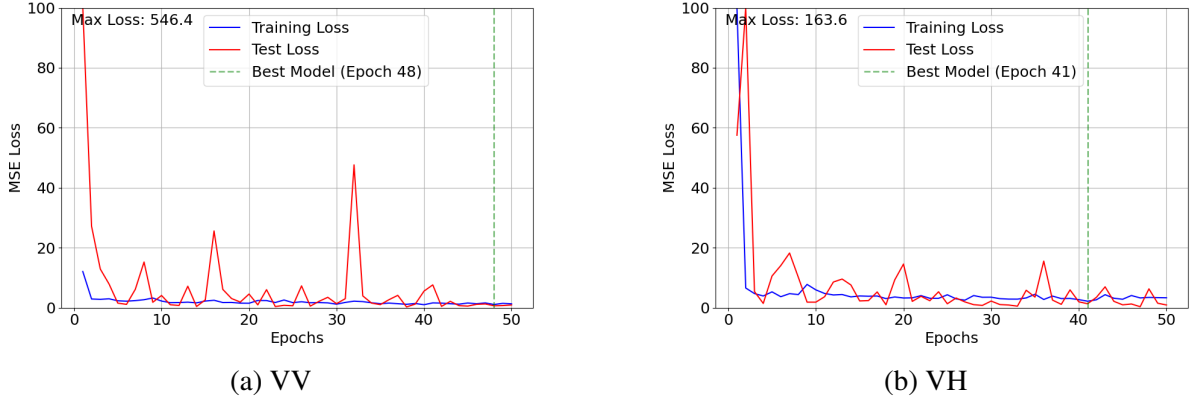


Figure 3.5: Train and test loss graphs for (a) VV and (b) VH polarization channels.

Table 3.1: Train and test performance metrics for VV and VH channels.

Metric (MSE)	VV (dB)	VH (dB)
Final Training Loss	1.3195	3.3288
Final Test Loss	0.9240	0.9298
Best Training Loss	1.0194	2.1891
Best Test Loss	0.2740	0.3544
Training Loss at Best Model	1.0983	2.1891
Test Loss at Best Model	0.6596	1.3439
Composite Score at Best Model	0.7431	1.3378
Best Model Epoch	48/50	41/50

Accurate estimation of SM and SSR through SAR backscattering is important for environmental monitoring and agricultural management. While the IEM has been widely used for simulating radar signals based on radiative transfer theory, its computational complexity and limited adaptability restrict its application. We presented a novel deep-learning framework that emulates IEM while maintaining an acceptable accuracy in both VV and VH polarized backscattering coefficients.

Chapter 4

Plant Schematics

4.1 Methodology and Data

Crop and soil specific parameters were collected through five field campaigns and same number of classes were created including bare soil and four crop growth stages. Field data collections were conducted at the same day that Sentinel-1 SAR acquisition over the wheat field that belongs to the NIRDPSB located at the following GPS location: 45°40'22.2"N, 25°32'28.1"E. ResNet-18 CNN was used to classify five stages of bare soil and crop growth stages and their corresponding average SAR backscattering from the ROI [36]. Each field campaign contains 10 measurement points inside a large wheat field and to cover variety of soil surface profile and dimensions of the wheat plants. At each measurement point we collected plant height and leaf length from two wheat crops, totaling 20 wheat crop data per growth stage. are detailed in Table 4.1. Only the plant stage-3 measurement campaign was performed one day after the satellite pass while all the others Sentinel-1 passed over the area of interest in the same day. The average plant height increases until the ripening (stages 1 to 3). The bare soil case is the first field measurement where we used a pinboard [13] to measure the SSR. Type of SSR used in this study is RR that is related to soil aggregate stability [37].

Table 4.1: The dates (all in 2023) and plant characteristics [cm] for the five in situ measurement campaigns [36].

Date	S0(24/03)	S1(25/05)	S2(09/06)	S3(30/06)	S4(27/07)
Min height	-	12.5	38.8	55.2	47.6
Max height	-	26	63.9	80.2	84.3
Avg height	-	19.8	52.3	69.2	64.4
Min # leaves	-	4	4	3	3
Max # leaves	-	7	7	4	4
Avg # leaves	-	5	5	4	4
Min leaf length	-	13.5	5	7	6.2
Max leaf length	-	26.1	25.1	26.1	31
Avg leaf length	-	19.2	16.8	18.1	16.8

Figure 4.1 illustrates real wheat crop images from each stage and their corresponding computer generated schematic forms. Height parameter of the cops have stem and head each measured separately, and in our image generation we distinguish them. Parameters of crops from each stage were used to create range and applied controlled randomness to generate more images than base samples per stage. Wheat plants have approximately 12.5 *cm* distance between each which is a perpendicular side view to the sowing direction and we calibrated our synthetic images to capture correct distance between canopies along with SSR profile. Wheat plants have curved leaves and to achieve this we used Bezier curve function.

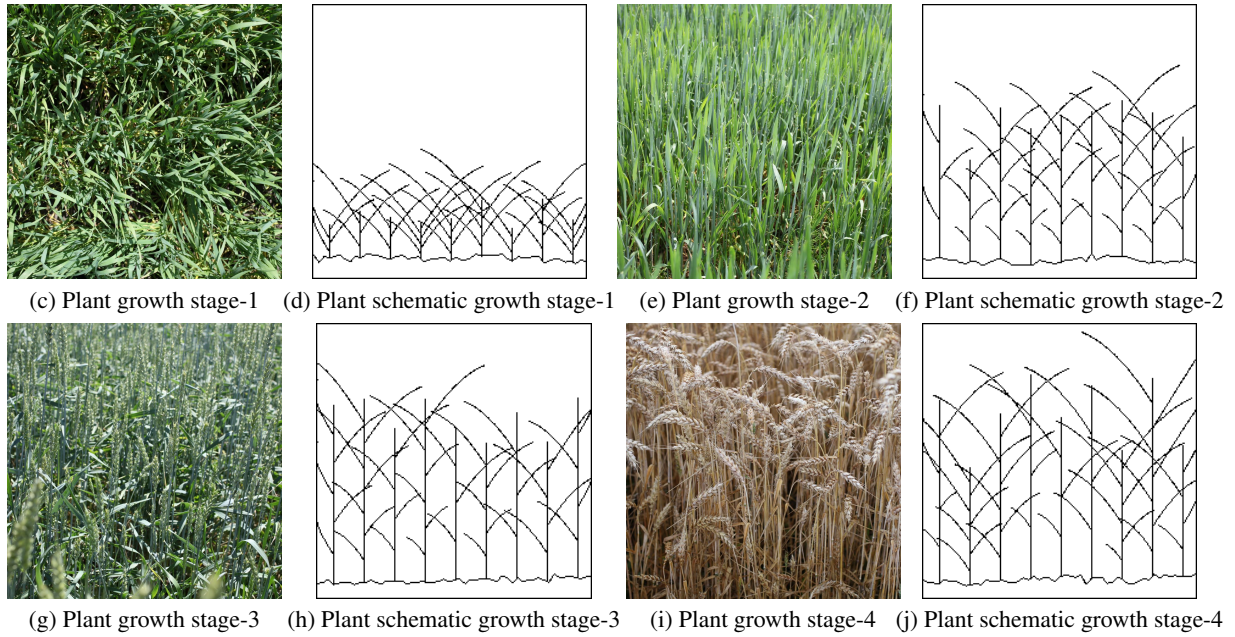


Figure 4.1: Plant growth stages [36].

Per stage including bare soil case, 1000 images were generated, a total of 5000 images. From these images, 80% of them were used for training and 20% for testing the model. However, we modified the input layer to receive one-channel binary images instead of three channels as default, output is also modified to classify images into five classes as opposed to the original 1000 classes. The model was trained and tested for 20 epochs with a learning rate of 0.0001 without any learning rate decay. We employed Cross-Entropy Loss for the classification task due to its effectiveness in multi-class scenarios, alongside the Adam optimizer for its adaptive learning rate features. We used average values of backscattering coefficients over the entire field from five campaigns as labels, each grouped to the 1000 images and these labels (target values) can be interpreted differently. The main interpretation is the classification of plant growth stages, which is obtained by associating Sentinel-1 backscattering coefficients with different plant growth stages that are identified through CNN. This approach is different from direct estimation of backscattering, as it uses classifications of generated plant schematics to infer backscattering values. Table 4.2 shows the minimum, maximum and average of Sentinel-1 backscattering values for each stage.

Table 4.2: Bare soil, four different wheat plant stages, and corresponding minimum and maximum backscattering (BS) coefficients [36].

Stage	Min BS (dB)	Max BS (dB)	Avg BS (dB)
Bare soil	-15.21	-11.79	-13.13
Plant stage-1	-14.73	-11.14	-13.49
Plant stage-2	-18.66	-13.09	-17.24
Plant stage-3	-13.46	-10.72	-11.91
Plant stage-4	-8.36	-5.87	-7.42

To obtain backscattering values SAR data needs to be processed and we used SNAP software to accomplish it while image generation and model training were implemented in Python. Sentinel-1 SAR data processing involves the following steps: calibration, speckle filtering, Range-Doppler terrain correction, and conversion of the band from linear to logarithmic (dB). Figure 4.2 illustrates the workflow from data collection to classification.

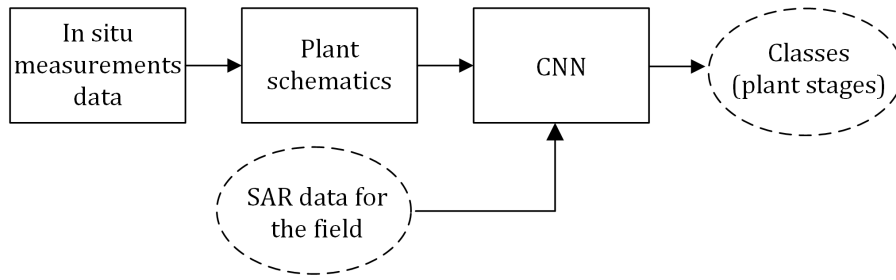


Figure 4.2: Block diagram of the workflow [36].

4.2 Results

K-density distribution of backscattering coefficients are shown in Figure 4.3 which suggests a weaker radar signature for stage-2 where crops are in early development stage, while backscattering values of other stages increase as the crops become bigger. Stage-2 shows overlapping behavior in radar signature with stage-1 indicating closer characteristics in wheat plants, however, overall distribution of the values still showing separation pattern.

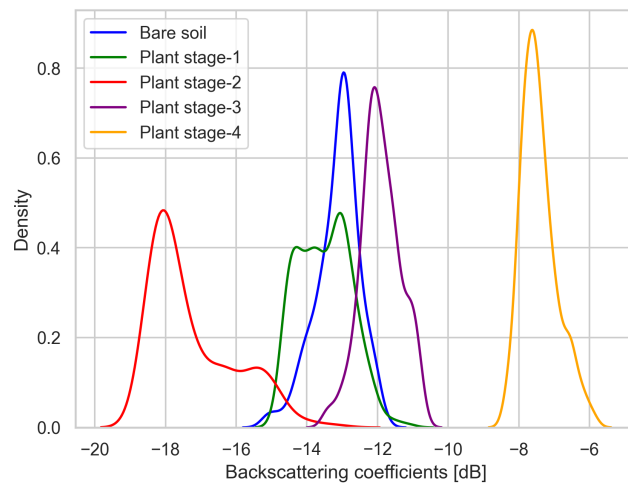


Figure 4.3: K-density estimation of backscattering coefficients [36].

Model achieves maximum of 100% accuracy on the training set and 96.4% accuracy on the test. The experiment shows potential in using CNN models for predicting the growth stages of plants and their signature on Sentinel-1 SAR. In the future by expanding the data and generating more detailed visual schematics, CNN models have the potential to predict a wider range of parameters.

Chapter 5

Hyperspectral Imaging: Visualization, Classification and Compression

5.1 Hyperspectral Image Visualization

One of the main challenges is the visualization of HSI due to the fact that HSI contain from tens to hundreds of bands but screens we are using display only three bands namely: red, green and blue. There are various ways to visualize HSI and significant amount of research has been done. Depending on the focus of the application, visualization method can be chosen, while some methods focus on most natural selection of RGB, others focus on highlighting the different materials in the scene. Proposed method includes two steps: (i) identifying the band and its wavelength value where maximum reflectance occurs. This involves selecting a single band out of tens or hundreds; (ii) assigning red, green and blue channel values to each identified wavelength per pixel. Matlab is for the implementation and described steps were illustrated and explained with more details in the following sections.

Identifying wavelength (λ) of the maximum reflectance band: This approach is performed on a pixel-wise basis by first determining the band with the maximum reflectance value (in nm). Figure 5.1(a) illustrates this step with a graph showing the maximum reflectance value of a pixel as 734 nm.

Pixel-wise conversion of a dominant wavelength to RGB color space values: We adopted the approach described in [38] to map the wavelength value to the RGB color space, computing the RGB color components as piece-wise linear functions of the wavelength λ . Figure 5.1(b) shows the functions used for assigning RGB values to each selected wavelength. For the RGB to wavelength conversion step, we utilized the lookup table to achieve faster execution of the proposed approach. The resulting colors as a function of wavelength (λ) are depicted in Figure 5.1.

5.1.1 Experimental Results

We used Pavia University hyperspectral data cube to experiment and test our method. This particular image was acquired with a Reflective Optics System Imaging Spectrometer (ROSIS) sensor and has a spatial resolution of 610×340 pixels and 103 spectral bands resulting in $610 \times 340 \times 103$ data cube. Sensor's spectral acquisition coverage ranges from 430 to 860 nm with step size of 4 nm. We dismissed the bands from upper end of the wavelength which were representing the infrared portion of the spectra, and used only visible part, thus, final data cube has $610 \times 340 \times 84$ dimensions. Experimental results of the proposed approach are shown in Figure 5.3 where we cropped the Pavia University Scene image into two parts, upper and lower to closely see the result of visualization. λ pseudo-image is the maximum reflected band's value.

From visualization results we can see that scene includes many shades of red, which is a consequence of the presence of natural materials such as bare soil, meadows, gravel, and trees. Artificial surfaces like asphalt and painted metal sheets appeared in blue like color (see Figure 5.3 (a) and (b)). Furthermore, shadows are emphasized with the violet color. Even though the main purpose of this approach to visualize

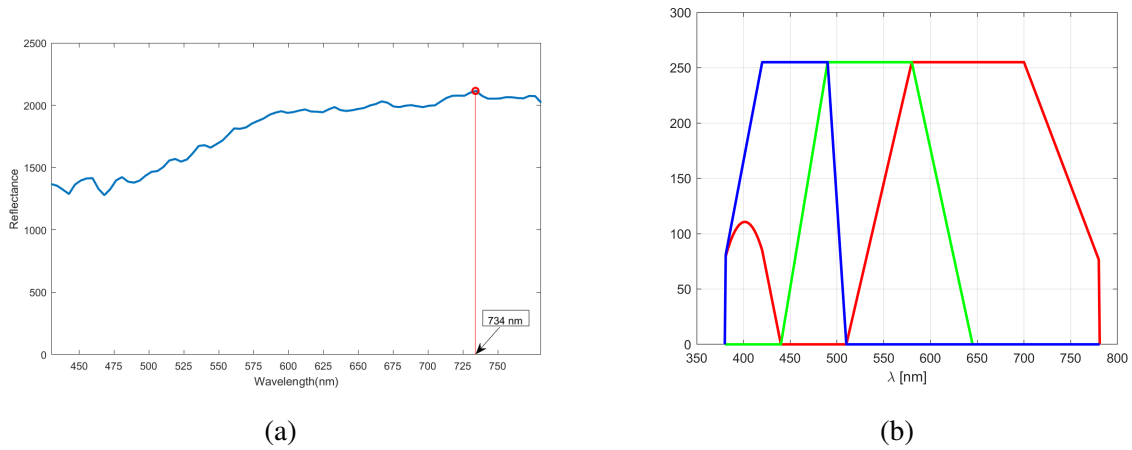


Figure 5.1: (a) A pixel spectral signature of Pavia University hyperspectral image and its maximum reflectance [39]. (b) Visual description of the functions for wavelength to RGB conversion [39].

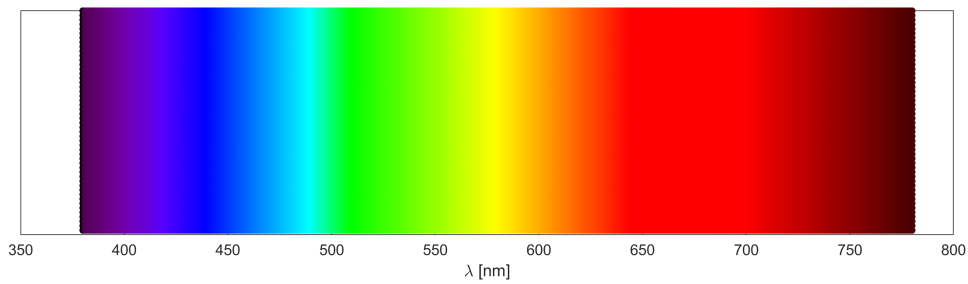


Figure 5.2: The colors in the visible spectrum as a function of wavelength (λ).

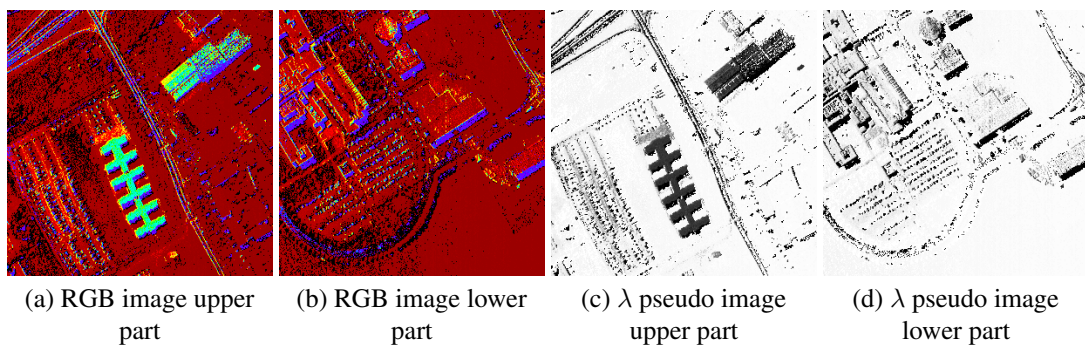


Figure 5.3: Experimental results of the proposed approach on Pavia University image crops [39].

the HSI it is clearly shown that it has potential to also perform pixel classification and segmentation in hyperspectral data. We utilized the Pavia University Scene dataset with its ground truth annotations. Our assessment focused on five distinct classes: meadows, trees, and bare soil (categorized as natural surfaces); painted metal sheets (representing artificial surfaces); and shadows (treated as a separate category). Table 5.1 presents the spectral wavelength ranges along with the percentage of correctly-classified pixels (PCCP) for each material type. The findings demonstrate the methodology's capability to accurately distinguish between the various surface types of materials present in the scene.

Table 5.1: Quantitative evaluation of correctly-classified pixels [39].

Samples	Painted metal sheets	Shadows	Natural surfaces
Range (λ)	470 – 550 nm	430 – 470 nm	620 – 780 nm
PCCP	99.5 %	94.2 %	99.8 %

5.2 Exponential Feature Extraction and Learning for Pixel-Wise Hyperspectral Image Compression

The compression methodology we propose relies on two fundamental hypotheses: adequate approximation of Fourier spectra of hyperspectral pixel reflectance profiles and negative exponential curve fitting to the transformed spectra; second, that ANN can effectively learn mappings between these negative exponential representations and actual spectral reflectance curves. Negative exponential function, ae^{-bx} captures essential spectral characteristics and results in a and b parameters which represents the compressed data, results in significant data volume reduction. Our second hypothesis benefits from recent ML advancements showing capacity of ANN model to model complex data relationships. The ANN model learns to map functional connections between compressed negative exponential representations and complete spectral reflectance profiles. Method achieves efficient hyperspectral image compression while maintaining information integrity. Our compression-decompression framework transforms each pixel's hyperspectral reflectance data $R(\lambda)$ using the Fast Fourier Transform (FFT). Due to symmetry properties, we retain only half of the FFT spectrum and model the amplitude by fitting a negative exponential function (see Figure 5.5 (a)). The resulting parameters (a , b) serve as our compressed pixel representation. For decompression, we train a neural network to reconstruct the original hyperspectral signature from these exponential parameters. To optimize the process, we discard near-zero values from the latter half of the vector before neural network processing. This compression-decompression pipeline is visually represented in Figure 5.4.

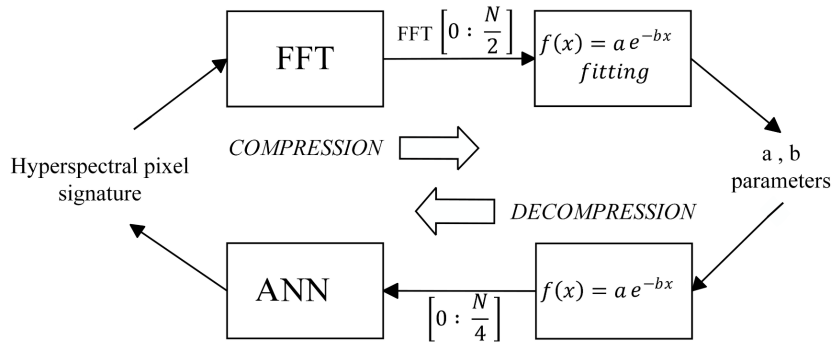


Figure 5.4: The block diagram of the proposed pixel-wise compression-decompression approach [40].

We designed and implemented a classical ANN with a single hidden layer, during decompression stage that predicts the true spectral reflectance curve of each pixel. Training is performed using a backpropagation algorithm with Adam optimizer, and the hidden neurons activate via the ReLU function. The networks architecture is modified to the characteristics of the hyperspectral image. For instance, the Pavia University Scene HSI contains 103 spectral bands. Initially, the FFT is applied, and number of bands reduced to 51 due to the symmetry; negative exponential function were fitted to the FFT and two coefficients (a and b) were extracted which represents the compressed data. During de compression phase, two coefficients were used to recover 51 values then another half of them disregarded due to the very small values on the other half. Final 25 values were used as input to the ANN. The output layer is configured with 103 neurons, matching the original number of spectral bands, while the hidden layer is

sized as the average of the input and output layers.

5.2.1 Experimental Results

The negative exponential features extracted from the Pavia University Scene hyperspectral imagery shows strong representation of the original data, as it is illustrated by the visual elements shown in Figure 5.5 (b) and Figure 5.6. When examining the correlation between these extracted features and the original data, the grayscale rendering Figure 5.6 (a) shows clear visual similarities to both the $\log(a)$ and b parameter pseudo-images in Figure 5.6 (b) and (c), respectively. Quantitative validation of these visual relationships are shown in Table 5.2, where Pearson CC between the extracted features and the original spectral information are present. The analysis reveals high correlation values, the $\log(a)$ parameter maintains coefficients achieved over 0.7 across all spectral bands, while the b parameter shows moderately strong relationships around 0.6. These statistical relationships confirm what visual inspection initially suggests: the negative exponential parameterization captures the essential characteristics of the hyperspectral data.

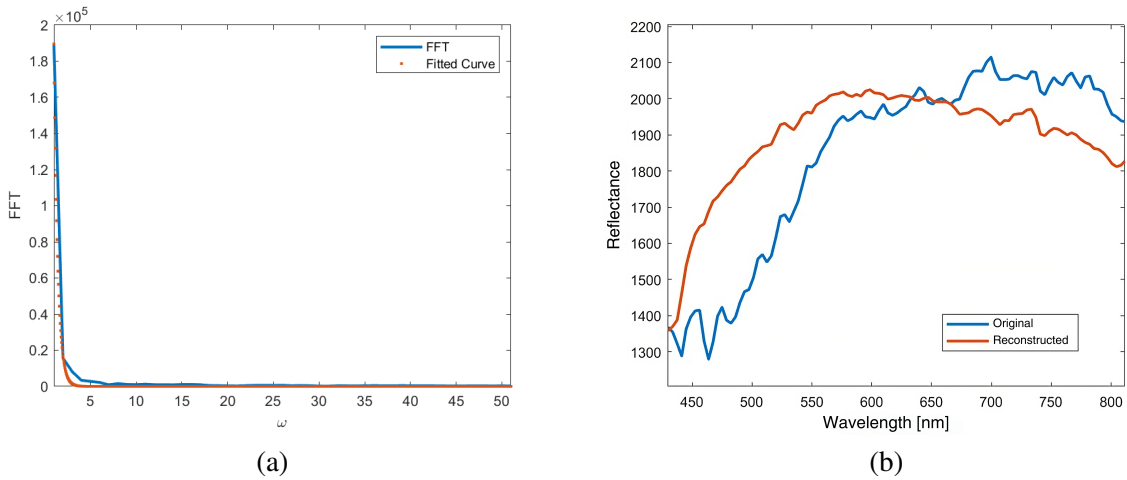


Figure 5.5: (a) Negative exponential curve fitted to the half FFT; (b) Original and reconstructed pixel spectral signature [40].

Table 5.2: Pearson CC between HSI band and $\log(a)$, b matrices [40].

Band	b_3	b_5	b_{21}	b_{25}	b_{50}	b_{60}
$\log(a)$	0.7	0.72	0.73	0.72	0.78	0.77
b	-0.58	-0.59	-0.58	-0.55	-0.59	-0.59

Spectral Angle Mapper (SAM) methodology from [41] measures pixel-by-pixel spectral similarity between the reconstructed and original hyperspectral data. SAM values predominantly cluster at the lower end of the scale, approximately 93% fall within the [0-0.2] range, while exhibiting an overall negative exponential distribution pattern with a mean value of 0.0817 and maximum reading of 1.2. These measurements provides two critical findings in our methodology: first, the negative exponential features successfully capture the characteristics of pixel reflectance curves' FFT representations; second, the ANN achieves high learning performance in mapping the relationship between features (a and b) and the corresponding spectral signature. The concentration of low SAM values indicates that the spectral reconstruction preserves the key information content of the original hyperspectral imagery with minimal distortion.

To visually assess reconstruction quality, we generated RGB composites of both original and reconstructed hyperspectral images using bands 53, 21, and 7 mapped to red, green, and blue channels respectively (see Figure 5.7 (a), (b)). After linearization for enhanced visualization, the reconstructed

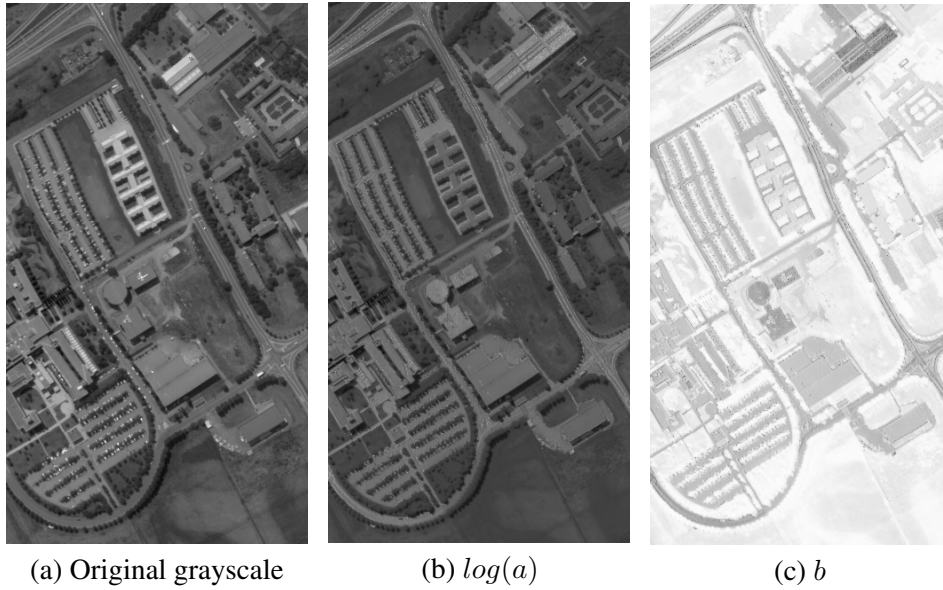


Figure 5.6: Experimental results of exponential decay feature extraction for the Pavia University Scene dataset [40].

image closely resembles the original, with minor color discrepancies primarily in metal roof regions. Quantitative evaluation used three metrics: Mean Absolute Error (MAE) [42], ΔE color difference [43], and Structural Similarity Index Measure (SSIM) [44]. For Pavia University dataset, we obtained $\text{MAE} = 3.71$, $\Delta E = 4.2$, and $\text{SSIM} = 0.97$, indicating high similarity. Figure 5.7 (c) displays the spatial distribution of ΔE color differences, revealing that most pixels exhibit $\Delta E < 20$, with 30% below the just-noticeable difference threshold of $\Delta E < 3$. Our pixel-wise compression approach achieved a compression ratio of 10.9967, reducing the original 33.1 MB Pavia University dataset to 3.01 MB of extracted features.

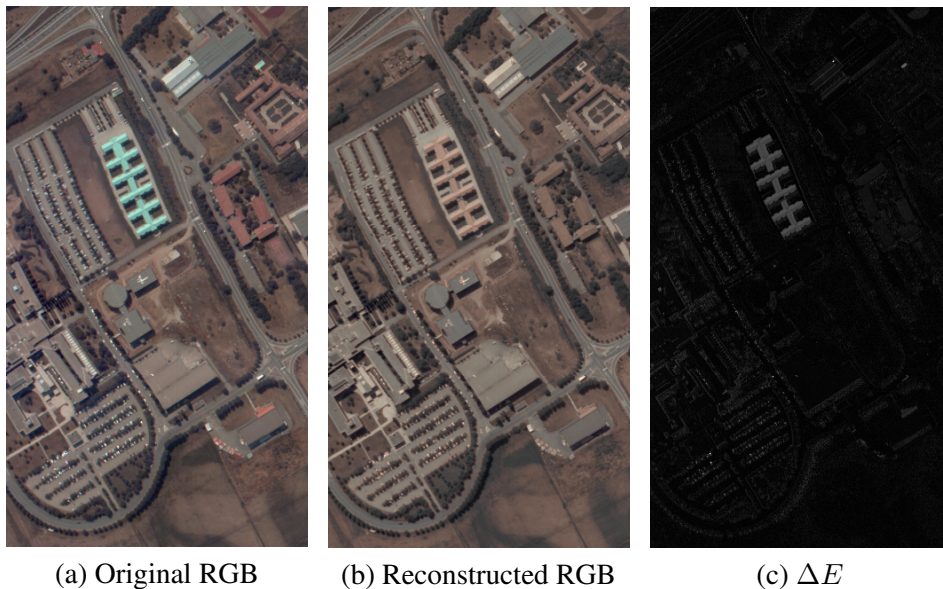


Figure 5.7: Original and reconstructed band-selection based RGB HSI image comparison along with ΔE color difference image [40].

Chapter 6

Crop Type Identification

6.1 Early Identification of Potato Fields Using Data Fusion and ANN

In order to test the hypotheses we used the images captured on May 23rd 2023 because in that day Sentinel-1 and Sentinel-2 data acquisition overlapped and ridging was present. ROI is Brasov, Romania and field boundary ground truth information was provided by the NIRDPSB. In Figure 6.1 a), one can see the ROI as RGB image while Figure 6.1 b) is the NDVI image computed based on the near-infrared (band-8) and red (band-4) channels of the Sentinel-2 image [45], while Figure 6.1 c) shows VH channel of SAR image. Polygons with magenta represent the potato fields while red ones represent the non-potato fields, more specifically, green peas, sugar beet, and corn crops which are used to train and test the ANN. The chosen potato fields have different potato types, but considered them homogeneous in our study because they do not present different patterns in ridging.

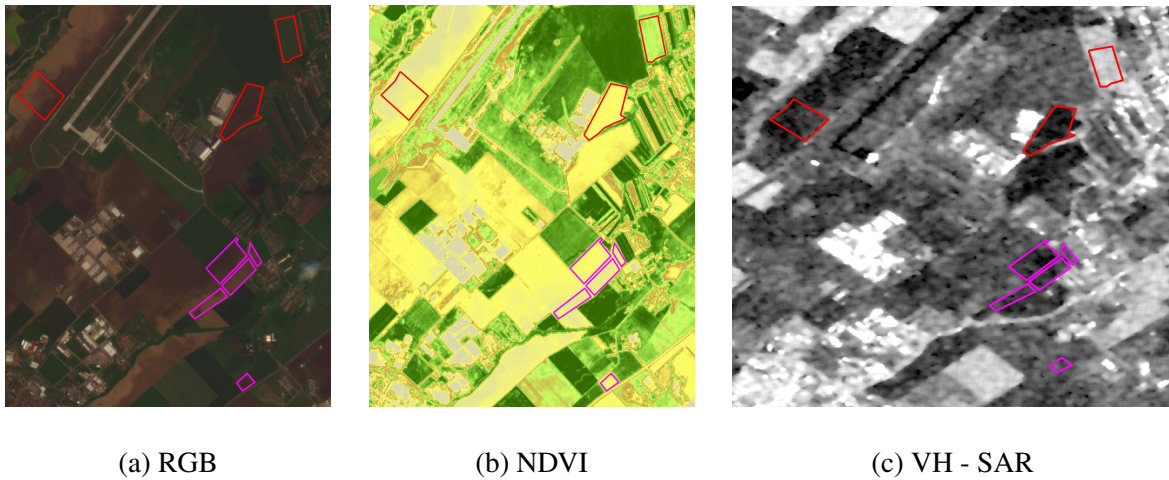


Figure 6.1: RGB and NDVI, from optical and VH channel from SAR image of the scene with polygons indicating potato (magenta) and non-potato (red) fields [46].

The fused dataset incorporates both multispectral and SAR data. From the multispectral data, it includes the first three principal components (PC1, PC2, PC3). and the NDVI. From the SAR data, it includes the backscatter coefficients $\sigma^0(VH)$, $\sigma^0(VV)$. The final contribution of multispectral data to the fused form contains PC1, PC2, PC3, and NDVI, and $\sigma^0(VH)$, $\sigma^0(VV)$ from SAR data. Then each pixel can be described as the following vector: $[\sigma^0(VH), \sigma^0(VV), NDVI, PC1, PC2, PC3]$.

6.1.1 Experimental Results

All the available Sentinel-2 images for the year 2023 were analyzed, Figure 6.2 shows the evolution of mean NDVI over five potato fields. A red highlighted period is the time of ridging operation, while

green indicates the potato crop growth. We implemented a feed-forward ANN with a backpropagation architecture consisting of two hidden layers containing 128 and 64 neurons respectively, each uses ReLU activation functions. The output layer is a sigmoid activation function that performs binary classification. We selected the Adam algorithm with a learning rate of 0.001 is used for optimization and training proceeded for 25 epochs with 64 batch size, using cross-entropy as a loss function. Extending training beyond 25 epochs produced no significant improvement in model accuracy. The dataset was shuffled prior to 80/20 split, with 80% allocated to the training set and the remaining 20% reserved for testing and evaluation. The end form of the data has a total of 5233 vectors, of which 36.52% represent potato fields and 63.48% represent non-potato ones. For our data processing pipeline, we used Python with the PyTorch framework to train and test the ANN, as well as to align and fuse the data. We employed SNAP ESA software for processing the multispectral and SAR images. As a result of training and testing over 25 epochs on two different datasets, we obtained high accuracy. Even though the main focus of the study is the identification of the potato fields at the preseason stage, we further trained and tested the same network on the dataset from the crop stage which is the fusion of Sentinel-2 acquisition at 12/07/2023 and Sentinel-1 at 11/07/2023. Table 6.1 shows the comparison of the accuracy results of training and testing from two dates. Higher accuracy on the second dataset can be explained by the fact that one of the features is NDVI which is prominent during the presence of the crops and less significant during preseason.

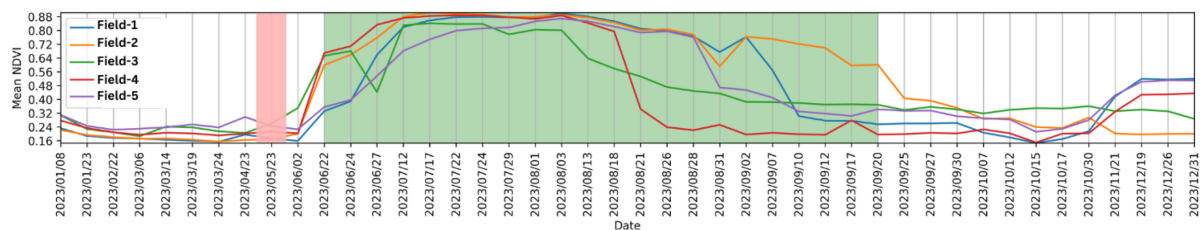


Figure 6.2: Mean of NDVI values from five potato fields [46].

Dates	Train Acc.(%)	Test Acc.(%)
Ridging (23/05/2023)	94.41	93.03
Vegetation growth (12/07/2023)	98	96.88

Table 6.1: Accuracy results from two different datasets [46].

Chapter 7

Conclusion

This thesis is interdisciplinary, bringing remote sensing, machine learning, and agriculture together, addressing challenges and problems in these fields. While a significant portion of it is dedicated to the applications in agriculture, HSI related chapter is broader. RS is a process of measuring the physical, chemical, and biological characteristics of the objects without physical contact. Instruments that measure the characteristics of an object remotely, can be carried in various ways such as simple attachment near the field, aircraft carriers, and satellite platforms. We used data from Sentinel-1 SAR and Sentinel-2 multispectral in some of our experiments while conducting multiple field campaigns and in-lab measurements for data collection. Data collection mainly included soil surface profiling with chain, and pinboard methods also known as classical methods, laser method and fractal analysis. We also captured multispectral images with drones for fractal analysis along with ones acquired on ground level. We collected data about wheat crop physical parameters during the growth season, covering all the stages of the development. Also generated synthetic images based on field data and simulated soil surfaces to estimate SAR backscattering. Ground data collection was not in RS fashion instead they were mostly contact methods in order to improve and develop RS techniques and tools. In collaboration with NIRDPSB, we had an opportunity to conduct field measurements also access to the ground truth labels of the field boundaries, ridging, and plant development timeline. The thesis also shows experiments and results regarding visualization, classification, and compression of hyperspectral data which are challenges not only in agriculture but in other domains as well.

Funded by the European Union, this thesis was developed under the AI4AGRI project. Romanian Excellence Center on Artificial Intelligence for Agriculture that aims to boost agricultural productivity and sustainability in Romania by leveraging AI and Earth observation data. As a first PhD thesis developed within the framework of a relatively new laboratory, it lays the foundation for future research and researchers.

Author Contribution

The main contributions are summarized as follows:

- Perform a performance evaluation of the classical methods for SSR assessment namely, chain and pinboard by conducting experiments in laboratory and in the agricultural field.
- Perform data acquisition over artificial and soil surfaces with laser, preprocessing and creation of data set. Train, test the ResNet-18 and evaluation of the results.
- Performed image alignment and other preprocessing steps of the the drone MSIs, application of FA and evaluation of the results.
- Designed an approach for generation of synthetic soil surfaces and SM with IEM. Creation of the dataset, design and implementation of CNN model and evaluation of the results.

- Design and implementation of determining maximum reflectance wavelength and conversion of it to RGB color space to visualize HSI image. Evaluation of the visualization method and results of pixel classification.
- Implementation of an approach to compress HSI data. FFT transformation of HSI spectra, curve fitting, as well as design, implementation of ANN, evaluation of training and test results in HSI data compression.
- Contribution to the realization of the a data set of radar (Sentinel-1) and optical (Sentinel-2) georeferenced data over 5 years for applications of crop identification and early crop identification.
- Design and implementation of data fusion technique between radar and optical data for the detection of potato crop ridges.
- Design and implementation of an approach for plant schematics image generation for plant growth stage and SAR backscattering coefficients classification.

List of Publications

1. M. Ivanovici, S. Popa, **K. Marandskiy**, and C. Florea. 2024. Deep Automatic Soil Roughness Estimation from Digital Images. *European Journal of Remote Sensing* 57 (1).
[doi: 10.1080/22797254.2024.2342955](https://doi.org/10.1080/22797254.2024.2342955). **Journal Paper, WOS:001208155100001, Q2, IF = 3.7**
2. M. Ivanovici, **K. Marandskiy**, G. Olteanu, A. Manea, and L. Dogar. 2024. A Framework for Innovation in Earth Observation Applications for Agriculture. *Bulletin of the Transilvania University of Brasov. Series I - Engineering Sciences*, November, 2136. [doi: 10.31926/but.ens.2023.16.65.1.3](https://doi.org/10.31926/but.ens.2023.16.65.1.3).
Journal Paper, Scopus
3. **K. Marandskiy**, M. Ivanovici and S. Popa, "Machine Learning-Based Classification of Sentinel-1 Backscattering Coefficients Using Generated Plant Schematics," *IGARSS 2024 - 2024 IEEE International Geoscience and Remote Sensing Symposium*, Athens, Greece, 2024, pp. 1535-1539,
[doi: 10.1109/IGARSS53475.2024.10640653](https://doi.org/10.1109/IGARSS53475.2024.10640653). **Conference Paper, IEEE Xplore, WOS:001316158501216**
4. M. Ivanovici and **K. Marandskiy**, "Exponential Feature Extraction and Learning for Pixel-Wise Hyperspectral Image Compression," *IGARSS 2023 - 2023 IEEE International Geoscience and Remote Sensing Symposium*, Pasadena, CA, USA, 2023, pp. 1775-1778,
[doi: 10.1109/IGARSS52108.2023.10282126](https://doi.org/10.1109/IGARSS52108.2023.10282126). **Conference Paper, IEEE Xplore, WOS:001098971602012**
5. M. Ivanovici, S. Oprisescu, R. M. Coliban and **K. Marandskiy**, "Exponential Features in the Fourier Domain for Prisma Hyperspectral Image Segmentation," *IGARSS 2023 - 2023 IEEE International Geoscience and Remote Sensing Symposium*, Pasadena, CA, USA, 2023, pp. 6089-6092,
[doi: 10.1109/IGARSS52108.2023.10282239](https://doi.org/10.1109/IGARSS52108.2023.10282239). **Conference Paper, IEEE Xplore, WOS:001098971606048.**
6. **K. Marandskiy** and M. Ivanovici, "Hyperspectral Image Visualization Based on Maximum-Reflectance Wavelength Colorization," *2023 17th International Conference on Engineering of Modern Electric Systems (EMES)*, Oradea, Romania, 2023, pp. 1-4,
[doi: 10.1109/EMES58375.2023.10171717](https://doi.org/10.1109/EMES58375.2023.10171717). **Conference Paper, IEEE Xplore**
7. **K. Marandskiy** and M. Ivanovici, "Soil Roughness Estimation Using Fractal Analysis on Digital Images of Soil Surface," *2023 International Symposium on Signals, Circuits and Systems (ISSCS)*,

- Iasi, Romania, 2023, pp. 1-4, [doi: 10.1109/ISSCS58449.2023.10190895](https://doi.org/10.1109/ISSCS58449.2023.10190895).
Conference Paper, IEEE Xplore.
8. **K. Marandskiy**, M. Ivanovici, S. Corcodel and S. Costache, "Multispectral Fractal Image Analysis for Soil Roughness Estimation at Various Altitudes," 2023 13th Workshop on Hyperspectral Imaging and Signal Processing: Evolution in Remote Sensing (WHISPERS), Athens, Greece, 2023, pp. 1-5, [doi: 10.1109/WHISPERS61460.2023.10431360](https://doi.org/10.1109/WHISPERS61460.2023.10431360). **Conference Paper, IEEE Xplore.**
 9. **K. Marandskiy** and M. Ivanovici, "Early Identification of Potato Fields using Data Fusion and Artificial Neural Network," 2024 International Symposium on Electronics and Telecommunications (ISETC), Timisoara, Romania, 2024, pp. 1-4, [doi: 10.1109/ISETC63109.2024.10797316](https://doi.org/10.1109/ISETC63109.2024.10797316). **Conference Paper, IEEE Xplore.**
 10. M. Ivanovici, G. Olteanu, C. Florea, RM Coliban, M. tefan, **K. Marandskiy** (2024). Digital Transformation in Agriculture. In: Ivascu, L., Cioca, LI., Doina, B., Filip, F.G. (eds) Digital Transformation. Intelligent Systems Reference Library, vol 257. Springer, Cham. [doi: 10.1007/978-3-031-63337-9_9](https://doi.org/10.1007/978-3-031-63337-9_9). **Book chapter, Springer.**
 11. M. Ivanovici, C. Florea, A. Caaron, R. Coliban, . Popa, I. Plajer, M. tefan, A. Bicoianu, . Opriescu, A. Racovianu, Gh. Olteanu, **K. Marandskiy**, A. Ghinea, A. Kazak, M. Debu, L. Majercsik, A. Manea, and L. Dogar. 2024. Teledetecie i inteligen artificial pentru agricultur. CARTOFUL în România, 33. **Journal Paper**
 12. **K. Marandskiy** and M. Ivanovici, "Early Identification of Potato Fields using Data Fusion and Artificial Neural Network," *Sensors*, MDPI [**Invited article**]. **Journal Paper, Q2, IF = 3.4**
 13. A. Bicoianu, I.C. Plajer, M. Debu, M. tefan, M. Ivanovici, C. Florea, A. Caaron, R. M. Coliban, . Popa, . Opriescu, A. Racovianu, Gh. Olteanua, **K. Marandskiy**, A. Ghinea, A. Kazak, L. Majercsik, A. Manea, L. Dogar, "DACIA5 A Sentinel-1 and Sentinel-2 Dataset for Agricultural Crop Identification Applications," *Big Earth Data*, Taylor & Francis [**In review, resubmitted**]. **Journal Paper, Q1, IF = 4.2**
 14. **K. Marandskiy**, L. G. Papale, M. Ivanovici and F. D. Frate, "A CNN-Based Approach for Understanding Sar Backscattering of Bare Soil," IGARSS 2025 - 2025 IEEE International Geoscience and Remote Sensing Symposium, Brisbane, Australia [**Accepted**]. **Conference Paper, IEEE Xplore, WOS.**

Bibliography

- [1] L. Thomsen, J. Baartman, R. Barneveld, T. Starkloff, and J. Stolte, “Soil surface roughness: comparing old and new measuring methods and application in a soil erosion model,” *Soil*, vol. 1, no. 1, pp. 399–410, 2015.
- [2] K. He, X. Zhang, S. Ren, and J. Sun, “Deep residual learning for image recognition,” in *Proceedings of the IEEE conference on computer vision and pattern recognition*, pp. 770–778, 2016.
- [3] S. I. Seneviratne, T. Corti, E. L. Davin, M. Hirschi, E. B. Jaeger, I. Lehner, B. Orlowsky, and A. J. Teuling, “Investigating soil moisture–climate interactions in a changing climate: A review,” *Earth-Science Reviews*, vol. 99, no. 3-4, pp. 125–161, 2010.
- [4] K. C. Kornelsen and P. Coulibaly, “Advances in soil moisture retrieval from synthetic aperture radar and hydrological applications,” *Journal of Hydrology*, vol. 476, pp. 460–489, 2013.
- [5] R.-M. Coliban, M. Marincas, C. Hatfaludi, and M. Ivanovici, “Linear and non-linear models for remotely-sensed hyperspectral image visualization,” *Remote Sensing*, vol. 12, no. 15, p. 2479, 2020.
- [6] Y. Dua, V. Kumar, and R. S. Singh, “Comprehensive review of hyperspectral image compression algorithms,” *Optical Engineering*, vol. 59, 2020.
- [7] I. Becker-Reshef, B. Barker, A. Whitcraft, P. Oliva, K. Mobley, C. Justice, and R. Sahajpal, “Crop type maps for operational global agricultural monitoring,” *Scientific Data*, vol. 10, no. 1, p. 172, 2023.
- [8] M. Weiss, F. Jacob, and G. Duveiller, “Remote sensing for agricultural applications: A meta-review,” *Remote sensing of environment*, vol. 236, p. 111402, 2020.
- [9] A. Orynbaikyzy, U. Gessner, and C. Conrad, “Crop type classification using a combination of optical and radar remote sensing data: A review,” *international journal of remote sensing*, vol. 40, no. 17, pp. 6553–6595, 2019.
- [10] G.-H. Kwak and N.-W. Park, “Impact of texture information on crop classification with machine learning and uav images,” *Applied Sciences*, vol. 9, no. 4, p. 643, 2019.
- [11] R. Yaramasu, V. Bandaru, and K. Pnvr, “Pre-season crop type mapping using deep neural networks,” *Computers and Electronics in Agriculture*, vol. 176, p. 105664, 2020.
- [12] A. Saleh, “Soil roughness measurement: chain method,” *Journal of soil and water conservation*, vol. 48, no. 6, pp. 527–529, 1993.
- [13] R. Allmaras, R. E. Burwell, W. E. Larson, R. F. Holt, *et al.*, “Total porosity and random roughness of the interrow zone as influenced by tillage,” *USDA Conservation Reserve Program*, 1966.
- [14] N. Cremers, P. Van Dijk, A. De Roo, and M. Verzandvoort, “Spatial and temporal variability of soil surface roughness and the application in hydrological and soil erosion modelling,” *Hydrological processes*, vol. 10, no. 8, pp. 1035–1047, 1996.

- [15] K. Marandskiy and M. Ivanovici, "Soil roughness estimation using fractal analysis on digital images of soil surface," in *2023 International Symposium on Signals, Circuits and Systems (ISSCS)*, pp. 1–4, IEEE, 2023.
- [16] M. Ivanovici, S. Popa, K. Marandskiy, and C. Florea, "Deep automatic soil roughness estimation from digital images," *European Journal of Remote Sensing*, vol. 57, no. 1, p. 2342955, 2024.
- [17] D. P. Kingma and J. Ba, "Adam: A method for stochastic optimization," *arXiv preprint arXiv:1412.6980*, 2014.
- [18] B. B. Mandelbrot and B. B. Mandelbrot, *The fractal geometry of nature*, vol. 1. WH freeman New York, 1982.
- [19] M. Ivanovici, "Fractal dimension of color fractal images with correlated color components," *IEEE Transactions on Image Processing*, vol. 29, pp. 8069–8082, 2020.
- [20] R. García Moreno, M. C. Diaz Alvarez, A. Tarquis, A. Paz González, and A. Saa Requejo, "Shadow analysis of soil surface roughness compared to the chain set method and direct measurement of micro-relief," *Biogeosciences*, vol. 7, no. 8, pp. 2477–2487, 2010.
- [21] W.-S. Chen, S.-Y. Yuan, H. Hsiao, and C.-M. Hsieh, "Algorithms to estimating fractal dimension of textured images," in *2001 IEEE International Conference on Acoustics, Speech, and Signal Processing. Proceedings (Cat. No. 01CH37221)*, vol. 3, pp. 1541–1544, IEEE, 2001.
- [22] M. Ivanovici, "A multi-spectral fractal image model and its associated fractal dimension estimator," *Fractal and Fractional*, vol. 7, no. 3, p. 238, 2023.
- [23] H. Bay, A. Ess, T. Tuytelaars, and L. Van Gool, "Speeded-up robust features (surf)," *Computer Vision and Image Understanding*, vol. 110, no. 3, pp. 346–359, 2008. Similarity Matching in Computer Vision and Multimedia.
- [24] K. Marandskiy, M. Ivanovici, S. Corcodel, and S. Costache, "Multispectral fractal image analysis for soil roughness estimation at various altitudes," in *2023 13th Workshop on Hyperspectral Imaging and Signal Processing: Evolution in Remote Sensing (WHISPERS)*, pp. 1–5, 2023.
- [25] J. R. Wang and T. J. Schmugge, "An empirical model for the complex dielectric permittivity of soils as a function of water content," *IEEE Transactions on Geoscience and remote sensing*, no. 4, pp. 288–295, 1980.
- [26] M. Choker, N. Baghdadi, M. Zribi, M. El Hajj, S. Paloscia, N. E. C. Verhoest, H. Lievens, and F. Mattia, "Evaluation of the oh, dubois and iem backscatter models using a large dataset of sar data and experimental soil measurements," *Water*, vol. 9, no. 1, 2017.
- [27] P. Dubois, J. van Zyl, and T. Engman, "Measuring soil moisture with imaging radars," *IEEE Transactions on Geoscience and Remote Sensing*, vol. 33, no. 4, pp. 915–926, 1995.
- [28] Y. Oh, "Quantitative retrieval of soil moisture content and surface roughness from multipolarized radar observations of bare soil surfaces," *IEEE Transactions on Geoscience and Remote Sensing*, vol. 42, no. 3, pp. 596–601, 2004.
- [29] A. Fung, Z. Li, and K. Chen, "Backscattering from a randomly rough dielectric surface," *IEEE Transactions on Geoscience and Remote Sensing*, vol. 30, no. 2, pp. 356–369, 1992.
- [30] N. Baghdadi, M. Zribi, S. Paloscia, N. E. C. Verhoest, H. Lievens, F. Baup, and F. Mattia, "Semi-empirical calibration of the integral equation model for co-polarized l-band backscattering," *Remote Sensing*, vol. 7, no. 10, pp. 13626–13640, 2015.

- [31] K. Chen, T.-D. Wu, L. Tsang, Q. Li, J. Shi, and A. Fung, "Emission of rough surfaces calculated by the integral equation method with comparison to three-dimensional moment method simulations," *IEEE Transactions on Geoscience and Remote Sensing*, vol. 41, no. 1, pp. 90–101, 2003.
- [32] A. K. Fung and K.-S. Chen, *Microwave scattering and emission models for users*. Artech house, 2010.
- [33] A. Fung and M. Chen, "Numerical simulation of scattering from simple and composite random surfaces," *JOSA A*, vol. 2, no. 12, pp. 2274–2284, 1985.
- [34] J. R. Birchak, C. G. Gardner, J. E. Hipp, and J. M. Victor, "High dielectric constant microwave probes for sensing soil moisture," *Proceedings of the IEEE*, vol. 62, no. 1, pp. 93–98, 1974.
- [35] C. Roth, M. Malicki, and R. Plagge, "Empirical evaluation of the relationship between soil dielectric constant and volumetric water content as the basis for calibrating soil moisture measurements by tdr," *Journal of Soil Science*, vol. 43, no. 1, pp. 1–13, 1992.
- [36] K. Marandskiy, M. Ivanovici, and S. Popa, "Machine learning-based classification of sentinel-1 backscattering coefficients using generated plant schematics," in *IGARSS 2024 - 2024 IEEE International Geoscience and Remote Sensing Symposium*, pp. 1535–1539, 2024.
- [37] I. Takken, "Effects of soil roughness on overland flow and erosion," 2000.
- [38] D. Miha and E. Strajescu, "From wavelength to r g b filter," *University" Politehnica" of Bucharest Scientific Bulletin, Series D: Mechanical Engineering*, vol. 69, no. 2, pp. 77–84, 2007.
- [39] K. Marandskiy and M. Ivanovici, "Hyperspectral image visualization based on maximum-reflectance wavelength colorization," in *2023 17th International Conference on Engineering of Modern Electric Systems (EMES)*, pp. 1–4, 2023.
- [40] M. Ivanovici and K. Marandskiy, "Exponential feature extraction and learning for pixel-wise hyperspectral image compression," in *IGARSS 2023 - 2023 IEEE International Geoscience and Remote Sensing Symposium*, pp. 1775–1778, 2023.
- [41] F. van der Meer, "The effectiveness of spectral similarity measures for the analysis of hyperspectral imagery," *International Journal of Applied Earth Observation and Geoinformation*, vol. 8, 2006.
- [42] Y. Hashidume and Y. Morikawa, "Lossless image coding based on minimum mean absolute error predictors," *Proceedings of the SICE Annual Conference*, pp. 2832–2836, 2007.
- [43] S. P. Farnand, "Using ΔE metrics for measuring color difference in hard copy pictorial images," in *Color Imaging VIII: Processing, Hardcopy, and Applications*, vol. 5008, pp. 109 – 118, International Society for Optics and Photonics, SPIE, 2003.
- [44] Z. Wang, A. Bovik, H. R. Sheikh, and E. P. Simoncelli, "Image quality assessment: from error visibility to structural similarity," *IEEE Transactions on Image Processing*, vol. 13, pp. 600–612, 2004.
- [45] J. W. Rouse, R. H. Haas, J. A. Schell, D. W. Deering, *et al.*, "Monitoring vegetation systems in the great plains with erts," *NASA Spec. Publ*, vol. 351, no. 1, p. 309, 1974.
- [46] K. Marandskiy and M. Ivanovici, "Early identification of potato fields using data fusion and artificial neural network," in *2024 International Symposium on Electronics and Telecommunications (ISETC)*, pp. 1–4, 2024.